CHALMERS
UNIVERSITY OF TECHNOLOGY

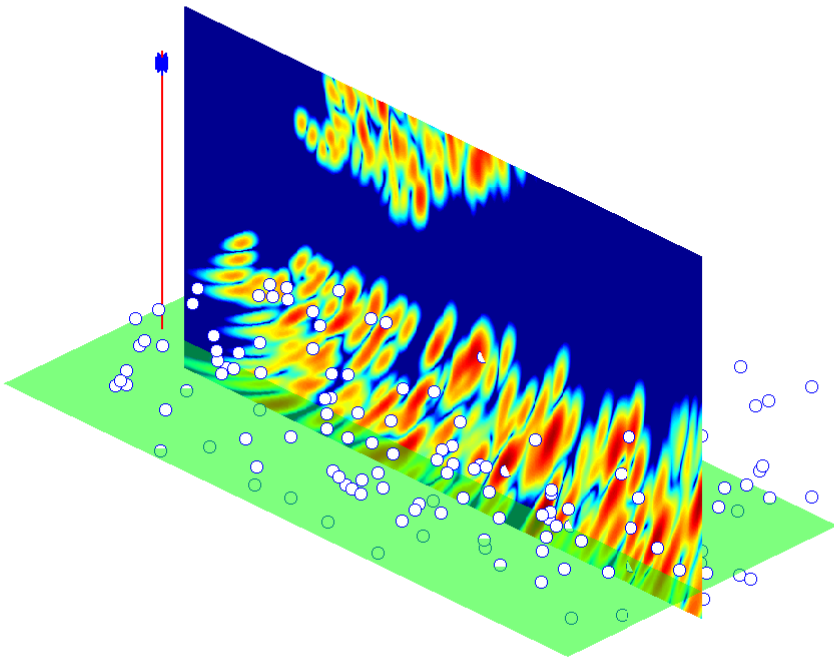

Fast factorised back-projection for reconstruction of tomographic images from bistatic radar measurements

Master's thesis in Wireless, Photonics and Space Engineering

MARTIN RÖNNFALK

Department of Space, Earth and Environment
Chalmers University of Technology
Gothenburg, Sweden 2018

Master's thesis 2018

Fast factorised back-projection for reconstruction of tomographic images from bistatic radar measurements

Martin Rönnfalk

CHALMERS
UNIVERSITY OF TECHNOLOGY

Department of Space, Earth and Envirionment
Division of Microwave and Optical Remote Sensing
Chalmers University of Technology
Gothenburg, Sweden 2018

Fast factorised back-projection for reconstruction of tomographic images from bistatic radar measurements
Martin Rönnfalk

Supervisor: Albert Monteith, Department of Space, Earth and Environment
Examiner: Lars Ulander, Department of Space, Earth and Environment

Master's Thesis 2018
Department of Space, Earth and Environment
Division of Microwave and Optical Remote Sensing
Chalmers University of Technology
SE-412 96 Gothenburg
Telephone +46 31 772 1000

Cover: Visualisation of a reconstructed image from simulated scatter targets in the geometry of the BorealScat radar tower.

Typeset in LaTeX
Gothenburg, Sweden 2018

Fast factorised back-projection for reconstruction of tomographic images from bistatic radar measurements

Martin Rönnfalk
Department of Space, Earth and Environment
Chalmers University of Technology

Abstract

The compelling evidence for climate change has increased the importance that we understand our environment and can properly model it to get factual prognoses. The carbon cycle is one part, of which there exists a large uncertainty in the land biomass, primarily forests. To improve our estimation abilities the BorealScat project is currently running, which consists of a tower based radar measuring the response from a forest. The data is used to reconstruct a vertical cross section image of the forest (tomographic image), thereby having another way to estimate biomass. The issue is that the processing of acquired data by the radar takes more time than the current measurement rate. Therefore this thesis investigates the possibility to implement a different reconstruction algorithm to decrease computation time.
The tower's full bistatic antenna geometry is simulated as well as a simpler monostatic approximation. For each of these a Global Back-Projection is implemented and used as a reference. The Fast factorised back-projection (FFBP) algorithm is implemented in the monostatic case, and partially implemented for the bistatic case (called BiFFBP). Simulated data and measured data were used for development and benchmarking of the algorithms.
A speedup fo 50% - 70% is achieved in the monostatic approximation case, which is of the same order as the theoretical maximum; four times speedup . The partial results for the bistatic case are demonstrated, however, time constraints hindered the completion of the implementation.
The conclusion is that the implementation of FFBP and BiFFBP show potential to help reduce the computational burden of the BorealScat project.

Keywords: radar, SAR, bistatic, back-projection, GBP, FFBP, BorealScat.

Acknowledgements

To begin with I would like to thank Lars for giving me the opportunity to do this interesting thesis at the division of Microwave and Optical Remote Sensing. Secondly I'd like to thank Albert for being a great supervisor and helping me understand many different aspects of the BorealScat project and system, making this a most valuable and worthwhile experience. A thanks to Jan who helped to improve my understanding of FFBP. I also thoroughly enjoyed the time spent in the thesis room together with the other thesis workers Johan and Victoria. The Friday fika with accompanied discussions and laughter was a well needed staple throughout this time.

Martin Rönnfalk, Gothenburg, 2018

Contents

1

Background

It comes as a surprise to few that climate change is a difficult problem that mankind is facing in the coming future [1]. In order for world leaders to make qualified decisions in policy making, models that can produce reliable forecasts are required. Great strides in this regard has been made and it can be shown almost without a doubt that human actions have contributed to climate changes [1]. In the modelling of climate change an important aspect is the flux of carbon, especially as part of the important greenhouse gas CO_2. The emission from burning of fossil fuels and absorption in the ocean can be quantified fairly well. However, there is a large uncertainty when it comes to the carbon cycle on land, mainly forests, where the in and out flux is derived from the other parts in the balance equation of total in and out fluxes and changing pools of accumulated carbon [2]. These indirect estimates are not satisfactory, and while there are methods for measuring biomass of forests they require a major effort of manual work, are destructive and/or time consuming, and therefore not applicable on a global scale [3].

To try and remedy this situation the European Space Agency (ESA) has approved the BIOMASS mission, which has the purpose to provide maps of stored carbon in the biomass of forests on a global scale, along with changes over time. The mission consists of a satellite with radar equipment that will utilize the scattering properties of forests to generate maps of estimated biomass density [2]. Synthetic Aperture Radar (SAR) techniques will be used to get all-weather capabilities and a higher resolution than real aperture imaging. In particular, the BIOMASS satellite will be the first one to use P-band frequencies for space-borne remote sensing (specifically 435 MHz and with a bandwidth of 6 MHz), which have the properties of being able to penetrate the canopy of forests and reflect off tree trunks and branches [4]. The satellite is planned to be run in three different modes; polarimetric SAR (PolSAR), interferometric SAR (InSAR), and a time-limited tomographic SAR (TomoSAR) mode. The launch is scheduled to take place in 2021 [5], and prior to that several projects are ongoing to help understand how the results from the satellite should be processed and interpreted. For example, there is currently insufficient understanding of how radar measurements over forests vary with changing weather and seasons. BorealScat is one such project that focuses on the temporal variations in radar measurements over boreal forests that are common in the northern hemisphere. Similar projects exist for other types of forest, such as TropiScat and AfriScat for tropical forests [6, 7].

1.1 Brief History of Radar and SAR

The history of radar starts less than 20 years after Heinrich Hertz experimentally proved the existence of electromagnetic waves [8], with the invention of an apparatus by Christian Hülsmeyer in 1904 that could detect ships in fog and bad weather in order to avoid collisions. Although this could not measure distance, and thus cannot claim to be the first radar, as the word initially was an acronym for RAdio Detection And Ranging [9]. Several people, including Tesla and Marconi, had hypothesised the idea of using electromagnetic waves to measure the distance to remote objects, but one of the first demonstrated cases of this is due to Robert Watson-Watt and Arnold Wilkins in the United Kingdom. Their efforts would later result in the famous early warning system Chain Home which provided the UK with an advantage against the german bombing raids during the second world war [10]. Although radar is still an important military technology it has developed and is applied to a multitude of civil areas, a few examples being traffic surveillance, measuring levels in tanks [11], and as is the case with this thesis, remote sensing.
A great step beyond the simple detection and ranging of radar was taken with the development of SAR. SAR is a high resolution technique that works by sampling the electromagnetic field of a scattered scene from multiple points, and thereby creating a synthetically larger aperture than the physical one. Through this technique SAR can compete in resolution with optical systems in certain cases. The first developments in SAR where made by C. A. Wiley in the early 1950's with the invention of Doppler Beam Sharpening (DBS). The first system using this technique was demonstrated in 1952, and with it the 100° beam width of a real Uda-Yagi antenna was reduced (sharpened) to about 1° [12]. Since then a continuous effort has improved both the theoretical understanding of SAR, and possible hardware implementation as well as processing techniques. It is also interesting to note that due to the fact that SAR was invented before fast computers where available, much of the early processing was done with optics. Today however, digital processing is the prevalent technology [13, 12].
Much of radar development has been motivated and driven by military and defence applications, with uses in other areas realised later. The topics in this thesis can certainly be used in a military setting, but everything that is developed here is for the BorealScat project as presented in Chapter 1.

1.2 SAR Modes

Besides the original intent of many radars to find metallic structures either in the air or at sea, an important use of radar is to image the ground. The most common mode comprises of a single transmit/receive antenna which is mounted fixed on a platform, usually an aeroplane or a satellite, and illuminates a strip as the platform moves. This is called stripmap mode SAR imaging and is illustrated in Figure 1.1. The spotlight mode is similar only that instead of the antenna being fixed it is rotated so to always point at a certain area [14].
With a single flight path only a two dimensional image can be obtained of the

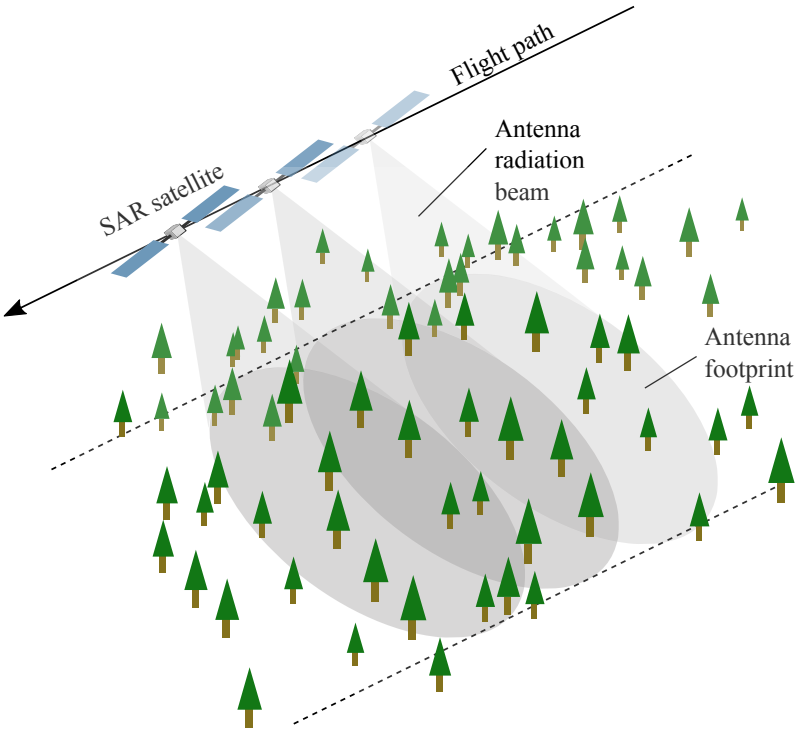

Figure 1.1: One of the simplest modes for SAR imaging is stripmap mode. Image courtesy of [3], reprinted with permission.

illuminated area, using two antennas or two fly-by's with different flight paths one can obtain topographic information of the area. This is called interferometric SAR (InSAR). Another mode is polarimetric SAR (PolSAR), where multiple polarisations are used to get more information.
A more recent idea is tomographic SAR (TomoSAR). It builds upon the principle of using multiple fly-by's, but instead of extracting topographic information with the assumption that scattering only happens at the surface, frequencies that penetrate the material is used to be able to create images with vertical resolution [15]. Figure 1.2 show the basic principle.

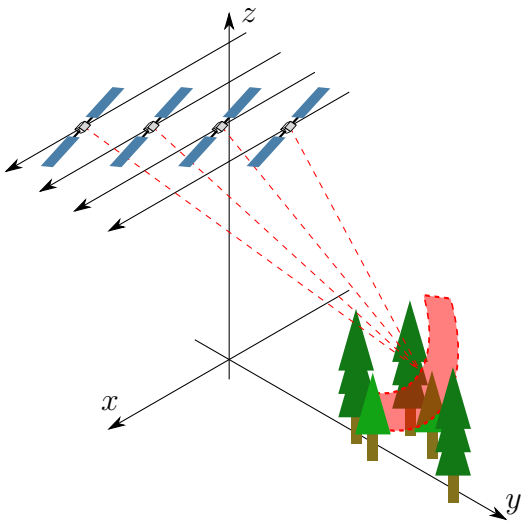

Figure 1.2: Tomographic SAR utilises multiple fly-by's in order to construct vertical cuts of the illuminated area.

1.3 The BorealScat Tower

The BorealScat project consists of a radar tower in Remmingstorp, Sweden, that overlooks a patch of boreal forest. This is monitored by SAR on a few different centre frequencies, f_c, and bandwidths, B, as specified in Table 1.1. The antenna arrays used are real arrays for all bands, although the terminology "synthetic aperture" will be kept throughout this thesis due to familiarity and consistency. For P- and L-band measurements the same 20-element antenna array is used, while for C-band there is a separate 10-element dual-polarised array. It is set up to capture data for reconstructing tomographic radar images on all bands with 5 min intervals [3].

Table 1.1: Centre frequency and bandwidth available for the BorealScat radar.

Frequency band		f_c [MHz]	B [MHz]
P-band	1	435	30
	2	514	8
	3	546	8
	4	640	56
L-band	5	1307.5	135
C-band	6	5410	320

Because of the large separation between the bands, and the desire to use the same, calibrated, equipment for all bands, a generic 20-channel Vector Network Analyser (VNA) is used instead of custom-designed radar hardware. The VNA works by stepping the frequency within the specified bandwidth and reading the scattering parameters, as such data is collected directly in frequency domain. More details in Section 2.3 [3].
This data is then transformed into time domain, where Global Back-Projection

(GBP) is used to create tomographic images. GBP is an accurate but computationally expensive algorithm.

1.4 Purpose and Goal of Thesis

The technical motivation for this thesis is to speed up the reconstruction of tomographic radar images by implementing a faster algorithm than GBP. The Fast Factorised Back-Projection (FFBP) algorithm is a good choice as it's a variant of GBP. The theoretical speed up depends on image size but GBP is proportional to $\mathcal{O}(N^3)$ while FFBP is usually $\mathcal{O}(N^2 \log_2 N)$ so for fairly large images the speed up is notable [16].
The end goal is therefore to assist in the processing of SAR data, specifically from the BorealScat project, but with the possibility to apply it on other data sets. Assuming that a working implementation will be used the environmental impact of this will be two fold, as both helping with the speed up analysis of the data, and reducing the energy used in the processing due to the increased computational efficiency.
To accomplish this, the main goal is broken down so that incremental progress can be tracked. Early on the focus is on the theoretical foundation, while later parts put emphasis on different implementations; a reference GBP, a monostatic FFBP approximation, and a bistatic FFBP.

2
Theory

In this chapter the theory of SAR is presented. First the basic principles of SAR algorithms, geometries, and details specific to the BorealScat tower. Then the signal model and GBP is derived, the principles of FFBP are presented, as well as resolution, ambiguities and changes needed for the algorithms to accommodate the bistatic geometry.

2.1 Synthetic Aperture Radar Processing

Reconstructing images from received SAR signals can be done in multiple ways. The parameters that dictate which algorithm is chosen often comes down to what approximations can be done, and if it needs to be done in realtime or not.
SAR reconstruction algorithms are mainly divided into two main categories; frequency-domain, and time-domain algorithms. As this thesis focuses on the time-domain algorithm of back-projection only a short description of frequency-domain algorithms will be presented. The first methods to reconstruct SAR images worked in the frequency domain, being DBS as previously mentioned, also called unfocused SAR. Further developments lead to a fully focused SAR algorithm, Range Doppler Algorithm (RDA), which often uses the Fresnel approximation, and later the Polar Formating Algorithm (PFA), which employs the approximation of plane waves (Fraunhofer approximation), as just a few examples. All of these have a range of validity, for example PFA is only valid for large distances and/or small angular dwell. The $\Omega - k$ algorithm is more general in that no assumption of the electromagnetic wave is done, but it requires a straight line for the aperture to be accurate. For more details on these algorithms refer to [13, 17].
The time-domain algorithms are usually different versions of back-projection, with GBP being the first to be introduced to newcomers. The perhaps even more straight forward algorithm is the Time Domain Correlation (TDC), which is simply a correlation process with the expected response of a point object at a certain distance [18]. The GBP and TDC do not impose any approximations. Due to this fact, these algorithms build upon Gabor's theory of holography which was acknowledged early in the history of SAR but could not be realized because of computational limitations [13]. The derivation of GBP from the principles of TDC will be presented in Section 2.3. Several variants of back-projection that offer speed up compared to GBP have been invented, among them being Local Back-Projection (LBP) [19], Fast Back-Projection (FBP) [20], quad-tree algorithm [21], and FFBP [16]. Only GBP and FFBP will be treated in this thesis.

2.2 Geometry

The usual geometry presented in most introductory books on SAR is akin to the fact that for the longest time the primary application of SAR, was to image the ground from an aeroplane. This is illustrated in Figure 2.1. In this setup the same antenna

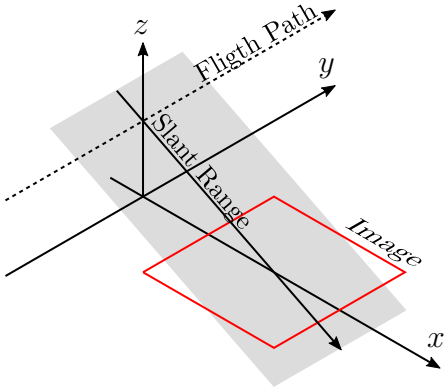

Figure 2.1: The usual geometry, where the xy-plane is the ground, z is height, and the slant-range plane, r, extends from the aperture path pointing to the middle of the image.

is used for both transmission and reception, i.e. the transmitter and receiver are co-located, which is called a monostatic geometry. A more general case is the bistatic geometry, where the transmitter is placed in a different location compared to the receiver. Making things even more general would be to consider multiple receivers for each transmitter, the multistatic case, which has the advantage that several cheaper passive receivers can utilize one more expensive transmitter. A historical note is also that the use of bistatic radar is older than the monostatic equivalent [22]. For most geometries that deal with moderate altitude and sizes of the aperture the approximation that the illuminated surface is planar is a good approximation, however, primarily for satellite radar this might not be the case. Instead both the curvature of the earth and the orbital track, as well as variable speed need to be accounted which complicates the geometry [23]. These are aspects that needs to be dealt with in the final case of the BIOMASS satellite, but for the tower radar in question it is not relevant.
A side view of the tower is shown in Figure 2.2. Already a distinction from the standard geometry in Figure 2.1 can be noted as the synthetic aperture extends vertically in the tower geometry in relation to the ground instead of horizontally. The reason for this is that the area of interest is the vertical distribution of backscatter in the forest and not an image of the illuminated plane, therefore in order to get a vertical cut (or average) the array is oriented in that fashion, as described in Section 1.2 [3].
If the antenna arrays are viewed from the front as in Figure 2.3 another distinction can be seen, i.e. that the geometry is bistatic. A picture of the real antenna arrays are shown in Figure 2.4. Pairing between the different polarisations is done to be able to extract more information from the forest, as for different transmit polarisa-

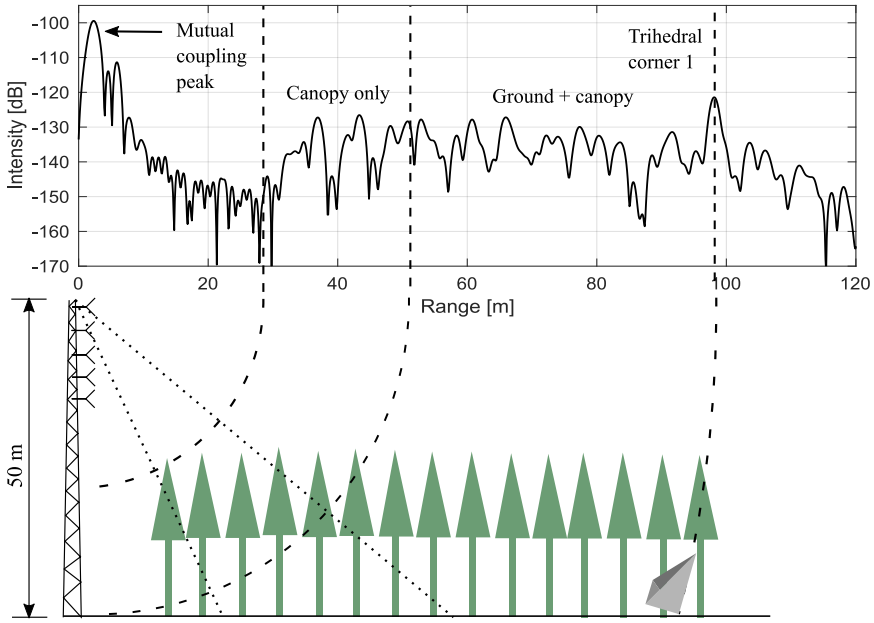

Figure 2.2: Side view of the tower and forest geometry, and what a generated signal, range profile, represent in terms of the physical scene. Image courtesy of [3], reprinted with permission.

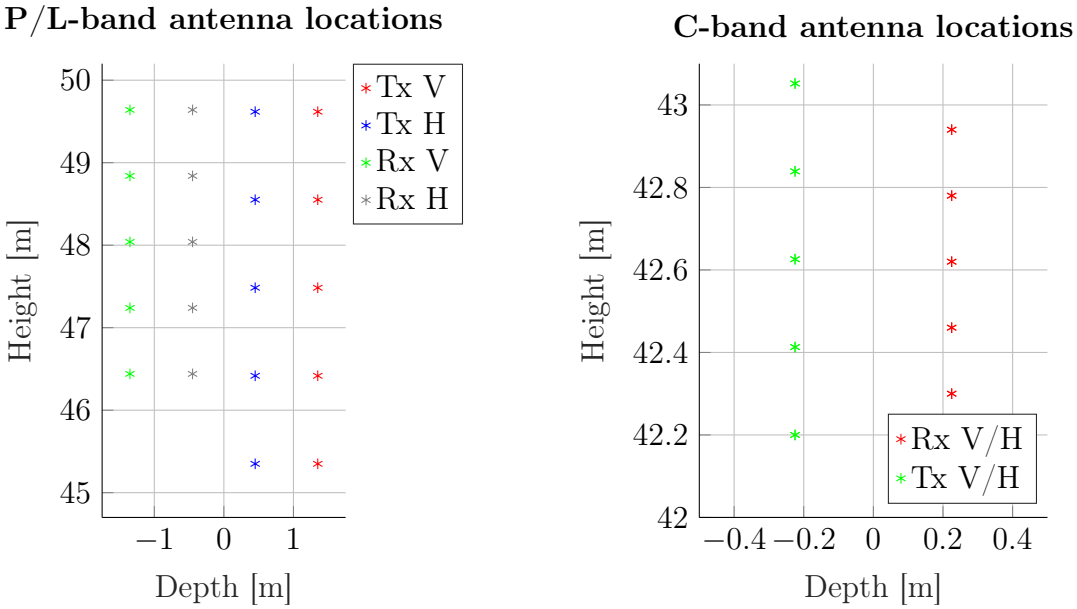

(a) The front view of the P/L-band antenna arrays with 20 elements, ten for each polarisation, where they are further divided into five for transmission and five for reception.

(b) Same view for the C-band antenna arrays, here with ten elements each being dual-polarised, and similarly five for transmission and five for reception.

Figure 2.3: Front view of the antenna arrays on the BorealScat tower.

Figure 2.4: Picture of the mounted antenna arrays. The pointy antennas are the P/L-band array, while the smaller rectangular shaped ones are the C-band array.

tion different scattering phenomena will occur [4]. Measurements and simulations for all combinations have been made. These being HH, VV, HV and VH where H stands for horizontal polarisation, V for vertical, the first letter indicates reception polarisation and the second letter transmission polarisation.

The image will be formed in the image plane which will extend in the middle between the transmit and receive arrays, an example of this plane is shown in Figure 2.5 with HH polarisation of the P/L-band antennas. In the monostatic approximation of the

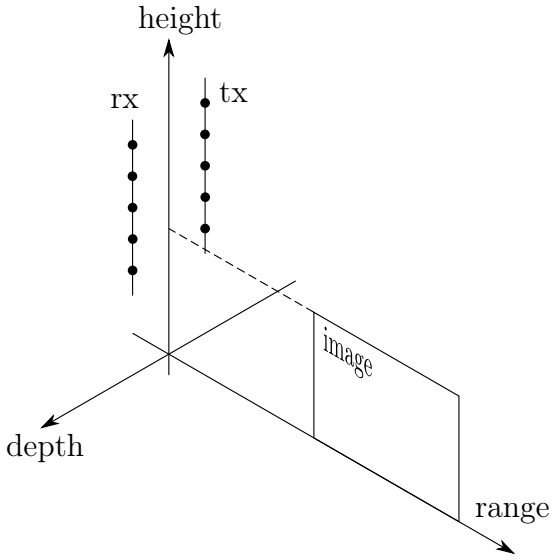

Figure 2.5: Example of the image plane for HH and VV polarisation of the P/L-band antennas.

bistatic case, that will be presented in Section 2.8, the virtual monostatic array will lie exactly between the transmit and receive aperture points, thereby will be in the image plane. Any distinction between the slant-range plane and image plane (or ground plane) disappears and all means the same. This will not be the case for the true bistatic geometry.

2.3 Signal Model and Global Back-Projection

As described in Section 1.3 the tower radar is utilising a VNA as transmitter and receiver, and the output from the VNA is in the frequency domain in form of S-parameter data. This is in contrast to the usual radar signal modelling approach, where a chirp (most simply a linear frequency modulation between two different frequencies) is often transmitted and then received with a quadrature receiver in order to create an approximate analytical signal [24].
Here follows a derivation of the GBP algorithm from first principles. The first step is to design a baseband signal, this can be a rectangular pulse, a shaped pulse, or more commonly in radar a chirp. To account for all possibilities an arbitrary complex signal is used, $s^{bb}(t)$, where bb stands for baseband. The signal is then in most cases up-converted to a higher frequency. There are multiple reasons for this, among them being that we're only permitted to transmit on a certain band, that the scattering phenomena to be observed only occur for certain frequencies, or to be able to construct a high gain antenna with reasonable dimensions. The up-conversion is usually represented in complex form in order to make the mathematical manipulations simpler.

$$s_{tx}^{pb}(t) = s^{bb}(t)e^{j\omega_0 t}$$

The notation pb indicates that it is a passband signal, and the real part of this is the signal that is transmitted by the radar system, which is indicated by tx. The carrier frequency f_0 is represented in $\omega_0 = 2\pi f_0$. The received signal is modelled as being scattered by a point scatter, indexed n, at a location determined by the delay t_n caused by back and forth propagation. The location will be in the two dimensional xy-plane as indicated by Figure 2.6. The point scatter approximation,

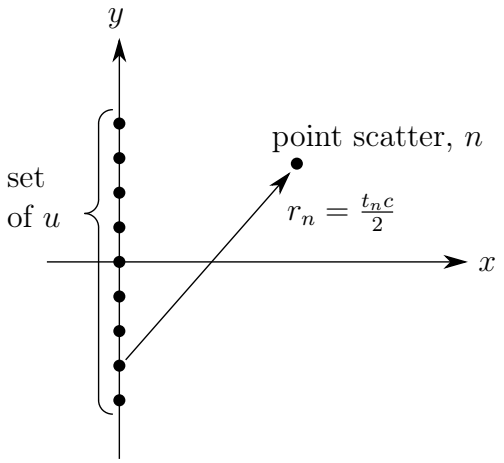

Figure 2.6: Geometry used in the derivation of GBP.

also called weak scatter approximation or the Born approximation [25], is needed to make the equations linear. This is more evident in the derivation of back-projection from Maxwell's equations, which is detailed in [26]. The received signal from a single

scatterer is

$$s_{rx}^{pb}(t) = a_n s^{bb}(t - t_n(t))e^{j\omega_0(t-t_n(t))} = a_n s^{bb}(t - t_n(t))e^{j\omega_0 t}e^{-j\omega_0 t_n(t)}$$

where a_n is the complex reflectivity of the point scatter. Free-space loss and antenna pattern dependent gain or loss are ignored for the time being but will be introduced in the simulation in Chapter 3. N scatterers can easily be modelled with

$$s_{rx}^{pb}(t) = \sum_{n=1}^{N} a_n s^{bb}(t - t_n(t))e^{j\omega_0 t}e^{-j\omega_0 t_n(t)}$$

Where N is the total number of scatterers to sum over. This complication will not be carried through in the derivation. The dependence of t_n on t comes from the possibility of the receiver moving during the receive window, or that the scatterer moves during the time it is reflecting the signal. For the tower's geometry the transmitters and receivers never moves, and while the trees of the forest can move under the influence of mainly wind, this effect will not be taken into account. However, this t dependence is still retained in order to later explain another approximation often used in SAR. The common situation is that the radar transceiver is mounted on a moving structure and thus t_n depends on t. The received signal is then down-converted back to baseband

$$s_{rx}^{bb}(t) = a_n s^{bb}(t - t_n(t))e^{j\omega_0 t}e^{-j\omega_0 t_n(t)}e^{-j\omega_0 t} = a_n s^{bb}(t - t_n(t))e^{-j\omega_0 t_n(t)}$$

The transceiver is moved along the synthetic aperture, which is indicated with u, which in the straight flightpath along an axis would be a scalar, but in the general case would be an arbitrary set of points in $\mathbb{R}^3$. Particularly in real applications where external factors can affect the path to deviate from a straight line, for example wind affecting an aircraft. In this derivation it will be limited to a straight path along one of the axis in a two dimensional geometry, e.g. u along the y-axis as in Figure 2.6. This creates a 2D signal space of range profiles, and to indicate the two dimensions another s is added to the function expression

$$ss_{rx}^{bb}(u,t) = a_n s^{bb}(t - t_n(u,t))e^{-j\omega_0 t_n(u,t)}$$

The full expression of $t_n(u,t)$ in the monostatic case is

$$t_n(u,t) = \frac{2\sqrt{x_n^2 + (y_n - u(t))^2}}{c}$$

and it is more clear how the position of u depends on fast-time, t. The 2 comes from propagation to the scatterer and back, and c is the speed of light. To get an estimate of the reflectivity of a scatterer at a certain location correlation is used between the received signal and a constructed reference signal which represents the signal a single scatterer would produce.

$$hh_{\mathbf{x}}^{bb}(u,t) = s^{bb}(t - t_d(u,t))e^{-j\omega_0 t_d(u,t)} \tag{2.1}$$

The reference signal is for an arbitrary point scatter at the location $\mathbf{x} = (x, y)$ in the xy-plane. And the time delay caused by the distance between $\mathbf{x}$ and u is t_d, defined as

$$t_d(u,t) = \frac{2\sqrt{x^2 + (y - u(t))^2}}{c} \tag{2.2}$$

The general cross-correlation, also called the *sliding inner product*, between two one dimensional equations, $f(t)$, $g(t)$ is defined as

$$(f \star g)(t) = \int_{-\infty}^{\infty} f^*(\tau) g(\tau + t) \mathrm{d}\tau$$

where the asterisks notation on f indicates complex conjugation. So by extending this to two dimensions the image can be reconstructed

$$I_{\mathbf{x}}(u,t) = \int_{-\infty}^{\infty}\int_{-\infty}^{\infty} ss_{rx}^{bb}(u+v, \tau+t) hh_{\mathbf{x}}^{bb*}(v,\tau) \mathrm{d}v\mathrm{d}\tau$$

However, for the usual radar geometry where the slant-range plane does not coincide with the image plane (or ground plane) makes the sliding inner product difficult to formulate. Therefore its more common to construct each pixel with their own $hh_{\mathbf{x}}^{bb}$, i.e. change it for each $\mathbf{x}$ [27]. To indicate that the $hh_{\mathbf{x}}^{bb}$ is specific to a certain pixel the subscript i is added, $hh_{\mathbf{x}_i}^{bb}$. Also doing a variable substitution $v \to u$, $\tau \to t$ gives

$$I_{\mathbf{x}_i} = \int_{-\infty}^{\infty}\int_{-\infty}^{\infty} ss_{rx}^{bb}(u,t) hh_{\mathbf{x}_i}^{bb*}(u,t) \mathrm{d}u\mathrm{d}t$$

for a single pixel at $\mathbf{x}_i$. Looping over all desired pixels would produce the image, and this algorithm is called Time Domain Correlation (TDC) [18]. The algorithm is very computationally intensive, on the order of $\mathcal{O}(N^4)$ for an $N \times N$ image with N aperture points. Therefore some approximations are introduced in order to make it more practically viable. Starting by inserting the expressions for $ss_{rx}^{bb}(u,t)$ and $hh_{\mathbf{x}_i}^{bb*}(u,t)$ gives

$$I_{\mathbf{x}_i} = \int_{-\infty}^{\infty}\int_{-\infty}^{\infty} a_n s^{bb}(t - t_n(u,t)) e^{-j\omega_0 t_n(u,t)}\ s^{bb*}(t - t_d(u,t)) e^{+j\omega_0 t_d(u,t)} \mathrm{d}u\mathrm{d}t \tag{2.3}$$

Instead of having a double integral the plan is to separate the compression of range and azimuth. For this to be achieved $ss_{rx}^{bb}(u,t)$ and $hh_{\mathbf{x}_i}^{bb*}(u,t)$ must be separable in range and azimuth, which the $t_n(u,t)$ and $t_d(u,t)$ dependence on t puts a stop to. However, if the transmitted signal is short, such that the movement of the transmitter and receiver is negligible, then the following approximations can be made

$$t_n(u,t) \approx t_n(u)$$
$$t_d(u,t) \approx t_d(u)$$

If the signal is not short and there is considerable movement during or between transmit and receive then displacement and/or blurring can occur if the approximation is used [28]. Note that if there is no motion of the transmitter or receiver, as is

the case with the tower geometry, as well as all scatterers staying stationary, then this is no approximation at all. Now eq. (2.3) can be written as

$$I_{\mathbf{x}_i} = \int_{-\infty}^{\infty}\int_{-\infty}^{\infty} a_n s^{bb}(t - t_n(u))e^{-j\omega_0 t_n(u)}\ s^{bb*}(t - t_d(u))e^{+j\omega_0 t_d(u)}\mathrm{d}t\mathrm{d}u \tag{2.4}$$

It can be shown that the process of correlation can be equivalently formulated using the technique of matched filtering [29]. The same is true for our SAR reconstruction case, and the matched filtering in range between the received signal and the reference is

$$\begin{aligned}(ss^{bb}_{rx} *_t hh^{bb*}_{\mathbf{x}_i})(u,\tau) &= \int_{-\infty}^{\infty} ss^{bb}_{rx}(u,t)hh^{bb*}_{\mathbf{x}_i}(u,t-\tau)\mathrm{d}t \\ &= \int_{-\infty}^{\infty} a_n s^{bb}(t - t_n(u))e^{-j\omega_0 t_n(u)}\ s^{bb*}(t - \tau - t_d(u))e^{+j\omega_0 t_d(u)}\mathrm{d}t\end{aligned}$$

Where $*_t$ indicates convolution over the fast-time variable t. For the pixel in question, $\mathbf{x}_i$, only the peak value is of any meaning, we therefore set $\tau = 0$, and the result is the same time integral as in eq. (2.4), i.e.

$$s^{bb}_{mf}(u) = \int_{-\infty}^{\infty} a_n s^{bb}(t - t_n(u))e^{-j\omega_0 t_n(u)}\ s^{bb*}(t - t_d(u))e^{+j\omega_0 t_d(u)}\mathrm{d}t \tag{2.5}$$

This is the range matched filtered response so to get the pixel value integration along the synthetic aperture is performed. Note that there is only a single s as it is one dimensional at this point

$$I_{\mathbf{x}_i} = \int_{-\infty}^{\infty} s^{bb}_{mf}(u)\mathrm{d}u$$

The common implementation is not to do the matched filtering integral for each pixel generating individual values, but do matched filtering on the entire signal, called pulse compression, then pick the relevant range sample. Also putting the reference phase factor outside the integration

$$\begin{aligned}ss^{bb}_{pc}(u, t_d(\mathbf{u})) &= (ss^{bb}_{rx} *_t ss^{bb*}_{\mathbf{x}_i})(u, t_d(u)) \\ &= \int_{-\infty}^{\infty} ss^{bb}_{rx}(u,\tau)\ ss^{bb*}_{\mathbf{x}_i}(\tau - t_d(u))\mathrm{d}\tau.\end{aligned}$$

Results in the pixel equation

$$I_{\mathbf{x}_i} = \int_{-\infty}^{\infty} ss^{bb}_{pc}(u, t_d(u))e^{+j\omega_0 t_d(u)}\mathrm{d}u. \tag{2.6}$$

It can be shown that this new algorithm has a computational complexity of $\mathcal{O}(N^3)$ which is an improvement from the TDC algorithm but still requires a fair amount of resources or time to reconstruct large images. The nature of SAR image reconstruction is an inversion problem, and for the rigorous mathematical treatment consult [30, 31].

The GBP and TDC have the advantage that they can inherently handle arbitrary flight paths [16], which the majority of the frequency domain algorithms can not. For them to be able to reconstruct images from aeroplane SAR data motion compensation is usually needed. Depending on algorithm different types of motion compensation might be desirable as well, e.g. for PFA motion compensation to a point is need, while for $\Omega - k$ it should be motion compensation to a line [13]. The frequency domain algorithms have still been more popular historically, not just due to being developed first, but also for the better computational efficiency. However, with the introduction of various new factorised versions of back-projection in the previous 20 years this advantage has diminished. Still, often the hardware is designed with a certain signal processing in mind therefore it might be difficult to implement a new algorithm for an existing platform. It should also be noted that GBP and other time-domain algorithms make the Nyquist requirements for an alias-free reconstruction somewhat transparent, i.e. it is easier to think one reconstructs an alias-free image but actually does not, compared to frequency domain algorithms where these requirements become explicit [13].
In the practical aspects of implementing GBP it works by projecting the range profile from each aperture point in spherical shells. This process is illustrated in Figure 2.7, with a two dimensional geometry. Between Figure 2.7c and Figure 2.7d it is clear that phase difference in the range profiles for different aperture points only interfere constructively for the pixel(s) where the scatter originated. From this description it is also clear that the same image would be constructed if the antenna would illuminate the other side of the synthetic aperture, even if there where no scatterers there. I.e. there would be an ambiguity and this is the reason SAR is usually side-looking.
A real digital system must deal with sampled signals in both fast and slow time. For slow time this means that the integral in eq. (2.6) becomes a sum over available aperture points, N

$$I_{\mathbf{x}_i} = \sum_{n=1}^{N} ss_{pc}^{bb}[u[n], t_d(u[n])]e^{+j\omega_0 t_d(u[n])} \tag{2.7}$$

where the square brackets indicates that the variable is discrete. Sampling in fast time implies that the pixel location is most likely between two samples in the range profile, and as such interpolation is needed before the pixel can be created.
Back-projection is often said to be a passband algorithm [13], and that the phase introduced by the downconversion needs to be compensated before processing and interpolation and then reinstated afterwards, however, this is only due to the fact that most interpolators work at baseband. There is no theoretical reason for why the phase can not be left and have the interpolator work at passband instead. It is convenient to use ready made interpolators, thereby making it necessary to modify the phase. Another reason to not work at passband is that it would require higher sampling.

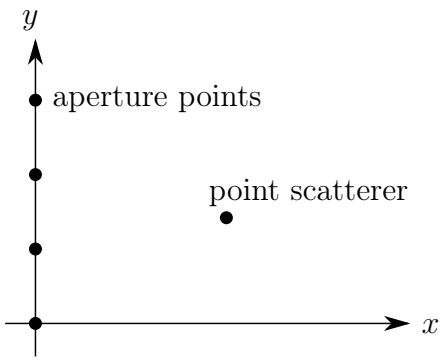

(a) 2D geometry with a 1D linear synthetic aperture and a single point scatterer.

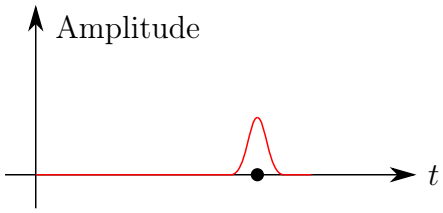

(b) Recorded range profile from one aperture point. The time at which the pulse is located corresponds to the distance between the scatterer and the aperture point via $r = {}^{tc}/_{2}$.

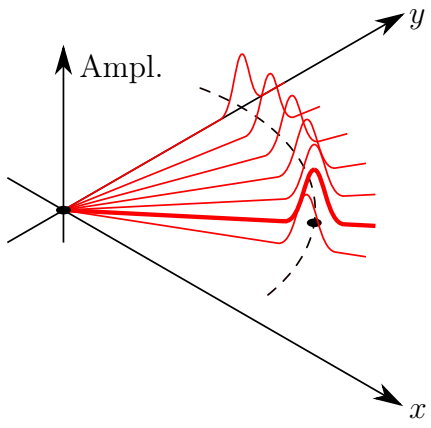

(c) A single range profile is plotted along an axis that coincides the point scatter. From the range profile data this location is unknown so spreading the range profile out in a circle covers all possibilities.

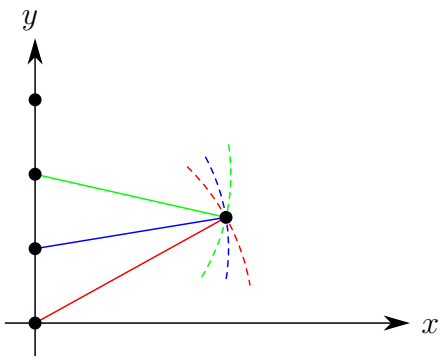

(d) If this is done for many aperture points they will line up only at the actual location of the point scatterer, and the phase of the complex samples will constructively interfere at that point.

Figure 2.7: The fundamental steps in the formation of a SAR image with GBP.

2.4 Fast Factorised Back-Projection

FFBP is a modification of GBP and a generalisation of previously developed modifications, such as [19, 20] and [21]. FFBP also goes by Direct Spherical Back-Propagation in some literature [13], the *spherical* here tells that only the monostatic case is considered.
The theoretical basis for FFBP is the realisation that it is unnecessary to back-project aperture data to all pixels for each new aperture position. If the back-projected data from two adjacent aperture points are visualised as in Figure 2.8 it can be seen that to a certain approximation the two aperture points can be represented by one range profile. One could also combine more than two aperture

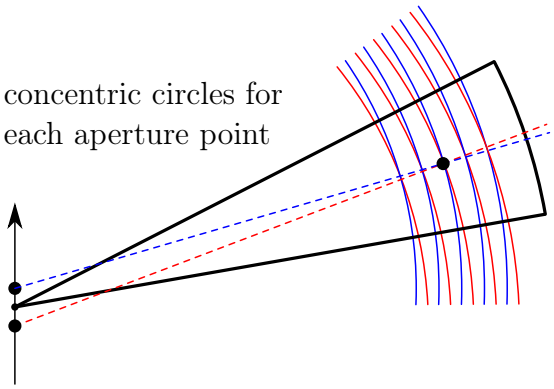

Figure 2.8: The data from two adjacent aperture points can be represented by a single range line within a certain angular extent because of approximately the same phase.

points, and then in order to not increase the error the angular extent that can be represented by a single range profile must be smaller. This is illustrated in Figure 2.9.

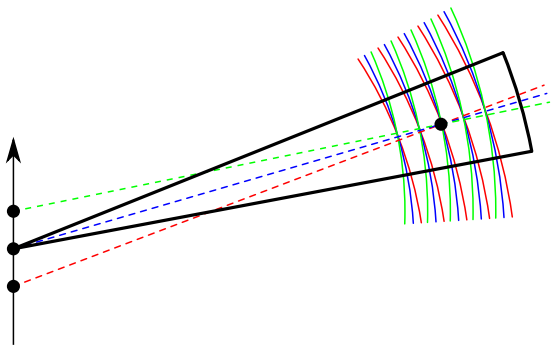

Figure 2.9: With more aperture points the corresponding beam can be viewed as being more narrow.

The algorithm works on the principle of splitting the synthetic aperture into these smaller subapertures, where a few aperture points are merged together. Then take

a few of these subapertures and merge to create larger subapertures, continuing this process until the full synthetic aperture has been assembled. The first steps of the process are pictured in Figure 2.10. From the geometry of algorithm formulation it

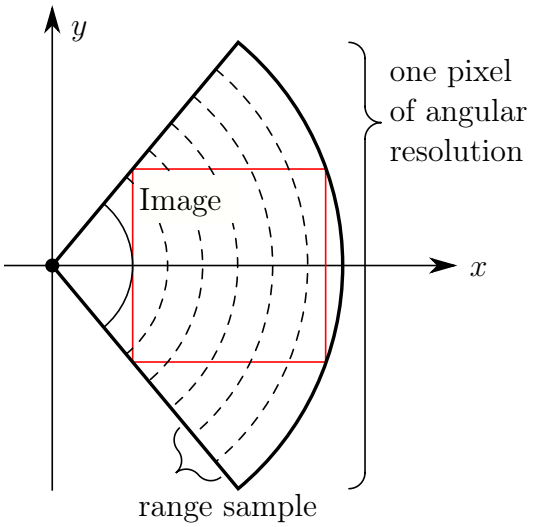

(a) The extent of which the data of one range profile covers the image plane.

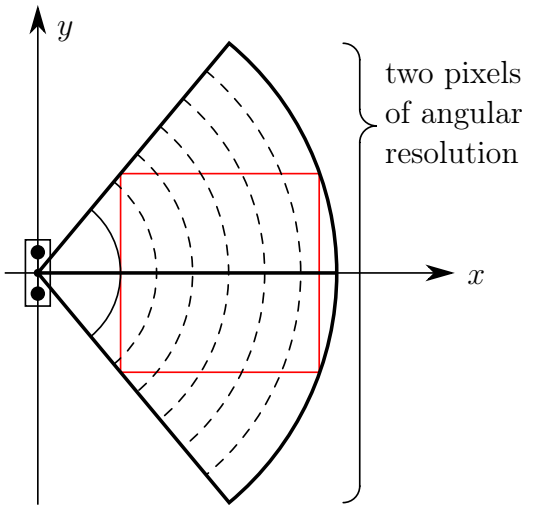

(b) The merger of two aperture points covering a large angular section, now the angular resolution is two.

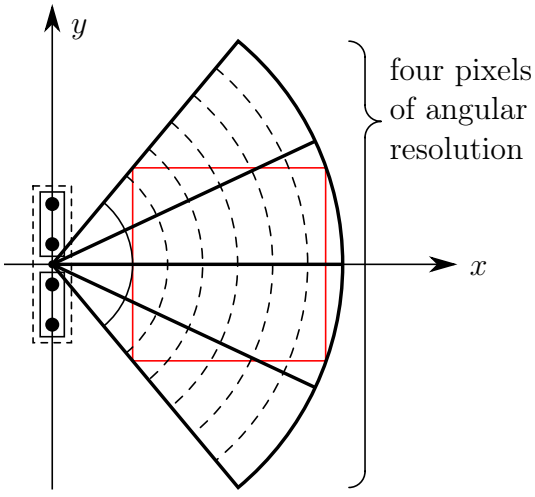

(c) The next step in the factorisation is to merge two subapertures, i.e. four aperture points. This results again in a doubling of the angular resolution, four pixels.

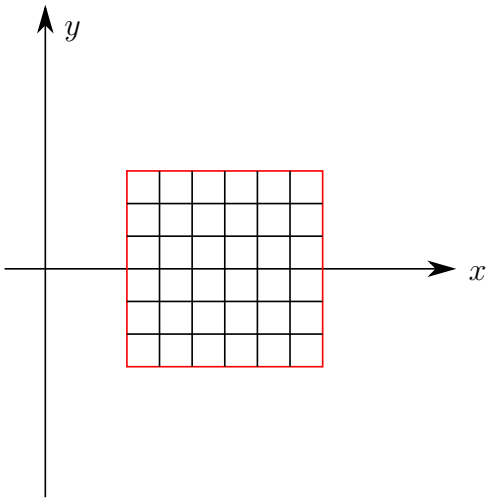

(d) After all aperture points are merged into one synthetic aperture the polar grid is interpolated to the final Cartesian grid shown here.

Figure 2.10: First steps in the procedure of FFBP.

is required to use a polar coordinate system as data is then uniformly distributed in radius and angle. In this version each step merges subapertures in pairs, reducing the number of subapertures by half, while also doubling the angular resolution with each step. This process is continued until the whole aperture has been merged. In the final step the polar image is interpolated into the Cartesian image coordinates.

The introduction of a new coordinate system for every subaperture with each step requires the data of the previous step to be interpolated to fit. Due to this interpolation errors are introduced which accumulate with each step in the factorisation.
It can be shown that the computational demand of the algorithm is $\mathcal{O}(N^2 \log_n N)$ for a N^2 image constructed from N aperture samples, merging n subapertures in each step of the algorithm. Most efficient is $n = 3$ but for the described number of virtual phase centres $n = 2$ is closer, and it provides only a 6 % loss in efficiency [16].
If the number of aperture points is not a power of two, range profiles could be discarded until only a power of two remains. Instead of discarding, it is better to use all information which can be done in a few different ways. The simplest would be to zero-pad with range profiles filled with zeros up to the correct amount. Another option would be to use GBP to reconstruct an image from the remaining range profiles and then merge that image coherently with the FFBP reconstructed one. Another approach would be to arrange so that all or most of the data can be used by using FFBP but with n changing between 2 and 3 at different steps as to fit the most number of range profile into the FFBP reconstruction as possible. This last method would probably be the most efficient, but was not implemented. Instead only a power of two number of aperture points are used for the reconstruction using a simple $n = 2$ approach.
As the number of aperture points in the case of the tower are far fewer than the number of pixels in the images, the speed up will not be as drastic as for the case of N aperture points for an N^2 image. Saying that we have A aperture points and reconstruct an $N \times M$ image with both GBP and FFBP the theoretical speedup is the ratio between the two

$$\frac{ANM}{NM \log_2(A)} = \frac{A}{\log_2(A)} \tag{2.8}$$

Which for $A = 16$ is 4. An increase smaller then this is expected to be achieved, due to various overhead.
Besides factorisation of the synthetic aperture another variant of FFBP also factorises the image domain and is described in [16]. Example implementation of both variants can be found in [32].

2.5 Stepped Frequency Waveform

As discussed in Section 1.3, a VNA is used for broadband capture of the radar signals from all bands. It uses a stepped frequency waveform to create a broadband signal, by short bursts of approximately monochromatic sinusoids with increasing frequency. An example of the waveform is plotted in Figure 2.11. The VNA does its processing so that in each of the bursts of monochromatic signal are approximated to be time-harmonic waves, i.e. steady state, and a complex sample to represent this is produced. The output of the radar measurement is therefore a part of the scattering matrix, each transmit/receive pair being a vector of complex samples over the specified bandwidth with the set spacing. However, the developed reconstruction algorithms work in time domain, which means that the frequency data needs to be

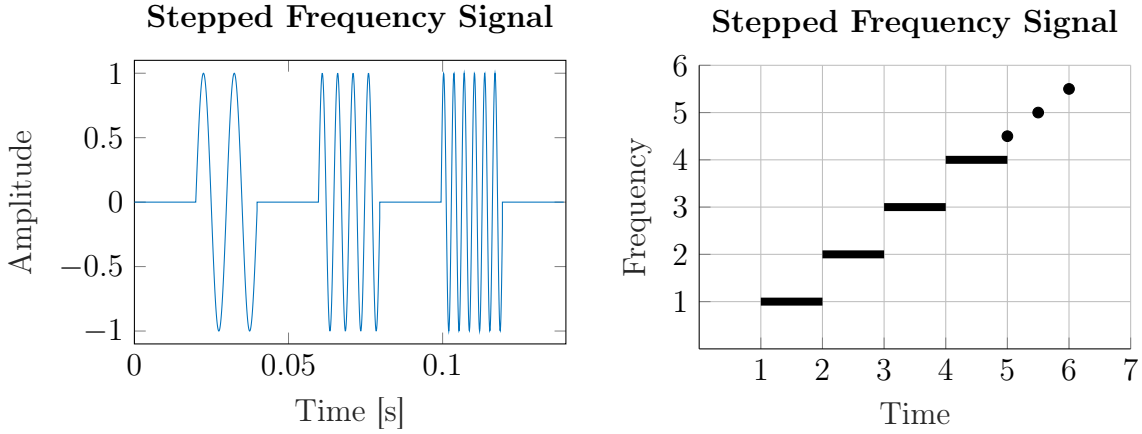

(a) Part of the stepped frequency signal in time domain.

(b) Shows how the time domain aspects of the signal relate to the frequency domain.

Figure 2.11: The stepped frequency signal, illustrated both in time-domain as well as combined time/frequency-domain.

inversely Fourier transformed such that the range profiles are recovered. In order to simulate the steady state at each step of the waveform this derivation will assume that it is a sinusoid that extends infinitely in time. That is to say that

$$s^{bb}(t) = e^{j\omega_i t}$$

where $\omega_i = 2\pi i \Delta f$ is the stepped frequency in baseband, with $i \in \{0, 1, 2, \ldots, N-1\}$ for N samples. Upconverting this to passband with carrier f_0 results in

$$s^{pb}_{tx}(t) = e^{j\omega_i t} e^{j\omega_0 t} = e^{j(\omega_0+\omega_i)t}$$

where $\omega_0 = 2\pi f_0$. It should be noted that in this formulation the carrier frequency used for upconversion is not the same as the centre frequency, due to the fact that the baseband signal is defined from 0 to bandwidth B, instead of symmetrically around zero frequency. A simulated received signal from a point scatterer at the distance r_n would be time-delayed, attenuated due to free-space loss, affected by the transmit and receive antenna patterns, A_{tx} and A_{rx}, as well as the scatterer's reflectivity, a_n:

$$s^{pb}_{rx}(t) = \frac{A_{tx} A_{rx} a_n k^2}{(4\pi r_n)^2} e^{j(\omega_0+\omega_i)(t-t_n)} \tag{2.9}$$

with $k = (\omega_0 + \omega_i)/c$, and $t_n = {}^{2r_n}/_c$ for the monostatic case. The scattering parameter that the VNA will generate, is defined as [33]

$$S_{21} = \frac{s^{pb}_{rx}}{s^{pb}_{tx}}$$

By inserting the expressions for s^{pb}_{rx} and s^{pb}_{tx} gives the following which conforms with literature [34]

$$S_{21} = \frac{s^{pb}_{rx}}{s^{pb}_{tx}} = \frac{\frac{A_{tx} A_{rx} a_n}{(4\pi r_n)^2} e^{j(\omega_0+\omega_i)(t-t_n)}}{e^{j(\omega_0+\omega_i)(t)}} = \frac{A_{tx} A_{rx} a_n}{(4\pi r_n)^2} e^{-j(\omega_0+\omega_i)\frac{2r_n}{c}} \tag{2.10}$$

This is the frequency-domain signal as measured by the VNA. As mentioned, in order to get the range profile we need to take the inverse Fourier transform of this data. It should be noted that it does not matter if baseband conversion of the signal would have taken place prior to extracting the scattering parameter, because it would have involved a $e^{-j\omega_0 t}$-term in both the numerator and denominator, cancelling each other.
The stepped frequency approach is a fairly slow one compared to other radar waveforms, therefore it is usually only used in lab environments or stationary platforms. The step-frequency technique also makes it possible to synthesise the response of any transmitted signal that is supported by the stepped-frequency signal in the frequency domain [26].

2.5.1 Pulse Compression

The technique of pulse compression is a standard topic in radar treatise [13, 26, 14, 35], and the application is mostly in terms of a linear chirp. For the idealistic case of range resolution one would want a Dirac delta function to be transmitted, reflected, and received. It would also be of interest to have a high transmit power as to be able to image further away, as the range depends heavily on this power because of the r^{-4} term in the radar equation [14]. Physical, technological, and legal limitations makes it impossible to send an arbitrary wideband, high power signal. A solution to this problem is instead to send a chirp which spreads out the frequencies in time, thereby putting more reasonable demands on the output power of the transmitter. The process of compressing the chirp into the tallest, thinnest pulse possible is called pulse compression, and is equivalent to a spectral phase shift. This is commonly implemented in terms of a matched filter, as that is the optimum filter that maximises Signal-to-Noise Ratio (SNR) of a signal in additive, white, Gaussian noise [35].
An advantage with the stepped frequency waveform is that no pulse compression is needed. As the frequency-domain samples are treated individually the phase can be matched arbitrarily which is done in real-time by the VNA hardware, thereby producing the same result as pulse compression.

2.6 Resolution

Resolution is one of the more important figures of merit in SAR. The common definition in SAR, and many other areas of physics where resolution plays a role, is the unit of measure needed to resolve two adjacent point objects. This is often called the Rayleigh resolution, and in SAR the natural unit is distance. The basic principles that lead to an increase in resolution are different in down-range and along-track respectively. In the geometry of the tower this is the same as range and elevation. For improvement in along-track (elevation) the imaged object needs to be illuminated from many different angles, this is illustrated in Figure 2.12. To get improvement in range one needs more bandwidth as explained in Section 2.5.1. Approximate equation for the resolution in range is

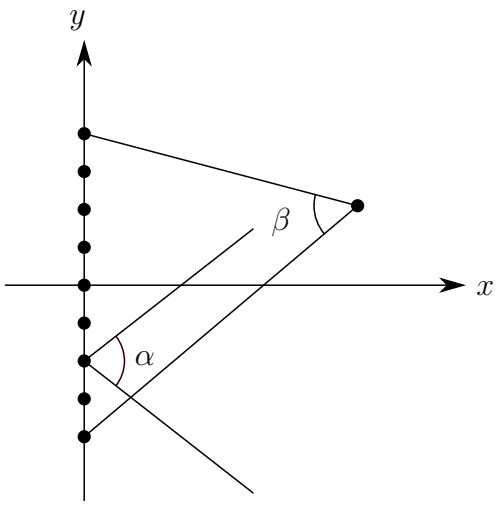

Figure 2.12: Synthetic aperture along the y-axis with the antenna beam width of α, gives that the total angular dwell, β, on a single point is limited by the beam width or synthetic aperture length.

$$\Delta r = \frac{c}{2B} \tag{2.11}$$

with c being the speed of light and B the double sided bandwidth at baseband [14, 36].
The resolution in elevation (along-track) at broadside can be approximated by

$$\Delta h = \frac{cr}{2f_c L} \tag{2.12}$$

at the range r, with centre frequency f_c, and synthetic aperture length L [37]. It is not uncommon to see that the cross-range resolution will be independent of range on the form of $L/2$, however, this is only applicable to certain situations and not with the tower geometry [13, 26, 14].

2.7 Ambiguities

In the common radar approach range ambiguities become a problem if during the receive window for a particular pulse the echo of the previous pulse is received due to a scatterer beyond the desired range. If the scatterer persists during many or all of the aperture points it will cause a local blurring because the hyperbolic range walk of that scatter will take on a different shape than is expected of the system for the place it appears in the range profiles.
In the VNA radar case these time-gated receive windows do not occur. Instead we fill the frequency spectrum directly causing maximum allowed range ambiguity based on how finely sampled this spectrum is according to

$$R_{amb} = \frac{c}{2\Delta f} \tag{2.13}$$

where Δf is the sampling spacing in frequency.
Ambiguities will also show up in elevation due to the discreteness of the synthetic aperture

$$H_{amb} \approx \frac{cr}{2f_c \Delta L} \tag{2.14}$$

with ΔL being the sample spacing in the aperture [36].

2.8 Bistatic Modifications

The monostatic setup for SAR has overall been more popular than bistatic or multistatic setups. This is mostly due to technical difficulties that appear when the transmitter and receiver(s) are located at different locations, such as time synchronisation, flight coordination, phase stability, and more [38].
Certain considerations must be taken into account when moving from a monostatic geometry to a bistatic one. For the GBP algorithm in Section 2.3 it was made clear that the collected range profiles should be distributed over equidistant pixels dependent on the range, with the aperture point in question as origin. These were spherical shells in the monostatic case, however, for the bistatic one this is no longer applicable. It can be shown that instead of spheres the equidistant surface becomes an ellipsoidal with one focus at the transmit position, and the other at the receive position. This is shown visually in Figure 2.13 for the case in two dimensions, but the same principle applies in three.

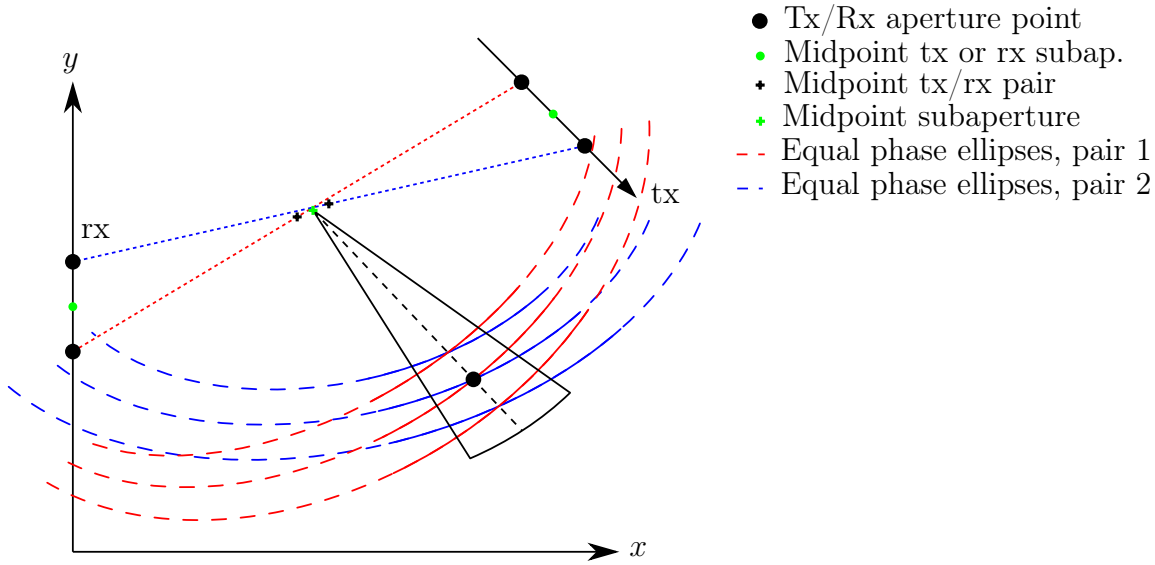

Figure 2.13: The bistatic geometry demands for an elliptic spreading of data instead of spherical, here in two dimensions, with the two black middle points as centres for the ellipses.

One approach to reconstructing images from data collected by a bistatic geometry is to approximate it by a virtual monostatic array placed in the middle between each transmit/receive pair [39]. In Figure 2.14 this approximation can be seen to

be valid for long ranges as it is the same as approximating the elliptical equidistant lines with a sphere, using a far-field approximation the match is exact. This virtual

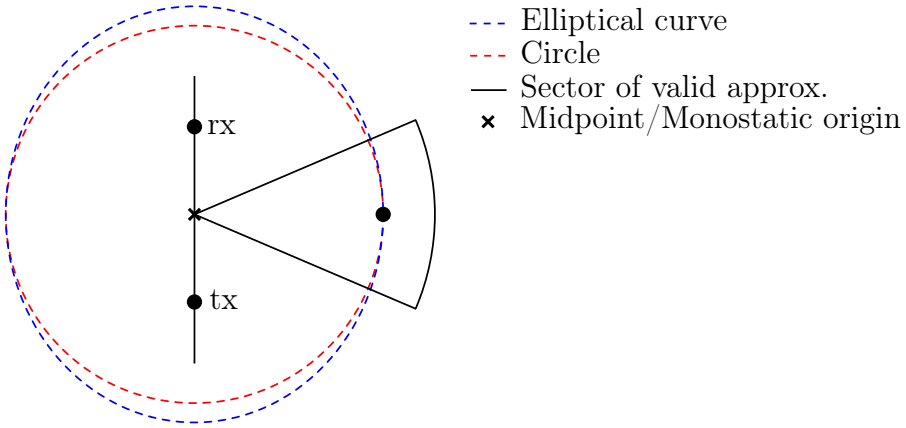

Figure 2.14: If the image lies in a small angular section it might be valid to approximate the bistatic geometry with a monostatic one, i.e. circular equidistant range instead of elliptical, positioned between the transmit and receive locations.

array will be employed in the simulation and compared to more approximation-free approaches, and be called the virtual phase array. The corresponding virtual ones for the P/L-band and C-band are plotted in Figure 2.15. Using this the same algorithms as defined for the monostatic geometry in Section 2.3 and Section 2.4 can be used for the bistatic geometry.

2.8.1 Global Back-Projection

In the bistatic version of the GBP no specific care has to be taken with regards to the ellipsoidal nature of the equidistant surface, rather just calculate the distance from the transmitter and receiver to the pixel being imaged individually. The equation for the pixel sum will be almost the same as eq. (2.7), but instead of just depending on the aperture position u it will depend on the transmit aperture position, u_{tx}, and the receive aperture position, u_{rx},

$$I_{\mathbf{x}_i} = \sum_{n=1}^{N} ss_{pc}^{bb}[u_{tx}[n], u_{rx}[n], t_d(u_{tx}[n], u_{rx}[n])] e^{+j\omega_0 t_d(u_{tx}[n], u_{rx}[n])} \tag{2.15}$$

The equation for t_d will also change from eq. (2.2) to

$$t_d(u_{tx}[n], u_{rx}[n]) = \frac{2}{c}(r_{tx}(u_{tx}[n]) + r_{rx}(u_{rx}[n])) \tag{2.16}$$

with r_{tx} and r_{rx} being the distance from the pixel to the transmit and receive location respectively

$$r_{tx}(u_{tx}[n]) = \sqrt{x_i^2 + (y_i - u_{tx}[n])^2}$$
$$r_{rx}(u_{rx}[n]) = \sqrt{x_i^2 + (y_i - u_{rx}[n])^2}$$

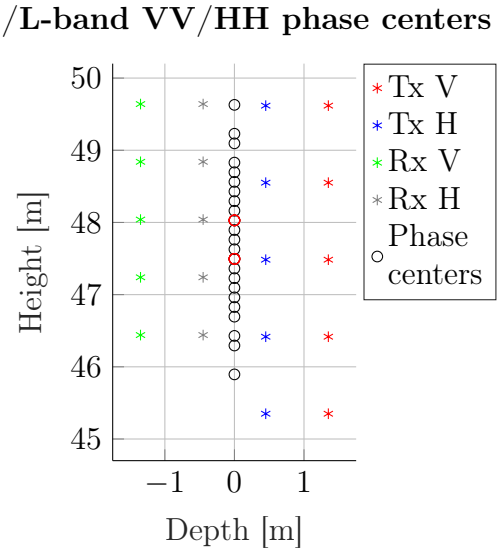

(a) Virtual phase centres for HH/VV polarisations of the P/L-band antennas. The red ring indicates that two aperture points are very close, almost overlapping.

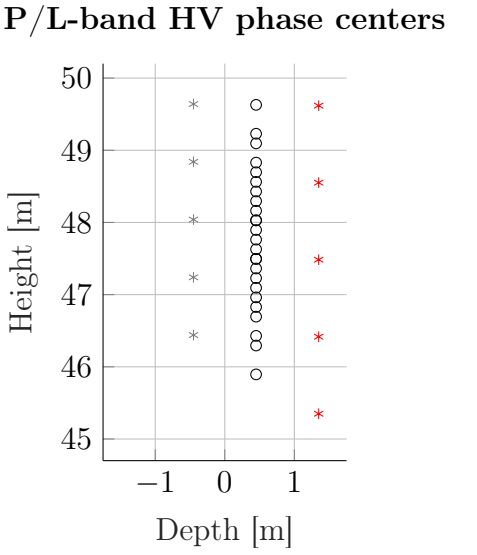

(b) Phase centres for the VH polarisation of P/L-band antennas. In this case there are also two pairs of overlapping aperture points, although these are not indicated in the plot.

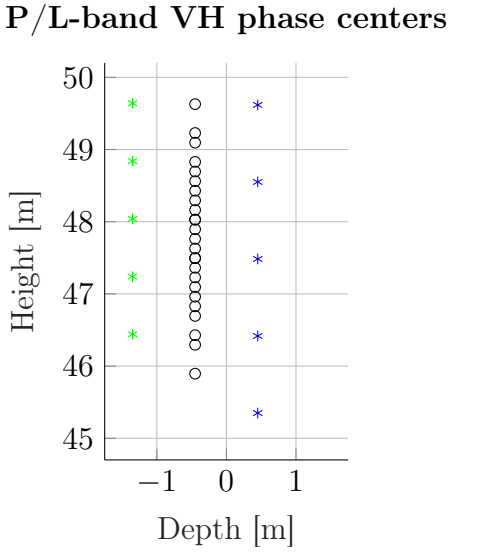

(c) Phase centres for the HV polarisation of P/L-band antennas. In this case there are also two pairs of overlapping aperture points, although these are not indicated in the plot.

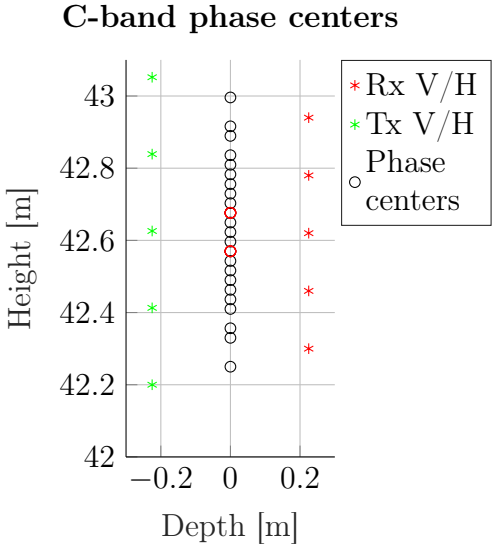

(d) Virtual phase array for all polarisation combinations of the C-band antennas. The same is true here, that the red rings indicates overlapping virtual apertures.

Figure 2.15: Virtual phase arrays for the different antenna configurations.

2.8.2 Fast Factorised Back-Projection

More modifications need to be made to the FFBP algorithm in order to make it work for the bistatic geometry. Two different methods have been presented in [40], of which the second one will be outlined and used here. The version of FFBP for the bistatic geometry will also be the polar one as was described in Section 2.4, and will be called Bistatic FFBP (BiFFBP) throughout this thesis.
The tower geometry is fairly specific, so to more clearly visualise how the algorithm works in general an arbitrary three dimensional setup will be analysed. Such a one is shown in Figure 2.16a, where there are two linear synthetic aperture arrays in the style of the standard geometry in Figure 2.1. Instead of formulating a polar coordinate grid that extends from the middle point of the array as in the monostatic case, now the origin is defined as the midpoint between the midpoints of the transmit and receive subaperture respectively. This is illustrated in Figure 2.16b, and then the grid is defined in the image plane, which in this case is the xy-plane. The grid is no longer polar but elliptical with foci at the location of the midpoints of the transmit and receive array project down onto said image plane. Two sets of these first subapertures are plotted in Figure 2.16c, and the next step in the factorisation is to combine these. Figure 2.16d shows the coordinate system of the merged subapertures with the refinement in angular resolution. As for FFBP this procedure is continued until the entire synthetic aperture is merged, and the final step is to interpolate from the elliptical grid onto a Cartesian one.
It should also be noted that FFBP have been applied in different bistatic scenarios before, examples being [41, 42, 43].

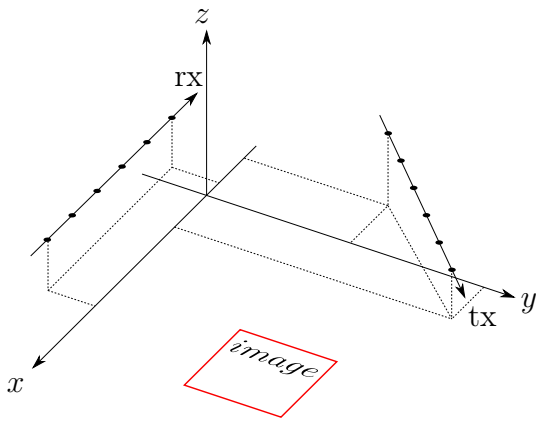

(a) Three dimensional bistatic setup with linear transmit and receiver arrays. xy-plane is the ground plane, with the image in this plane.

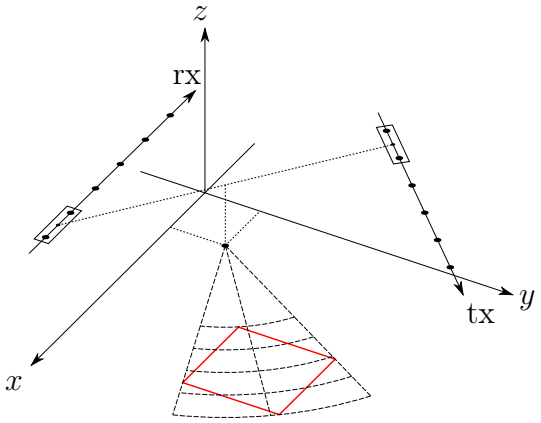

(b) The merger of two aperture points to a first stage subaperture. The origin is defined in the ground plane.

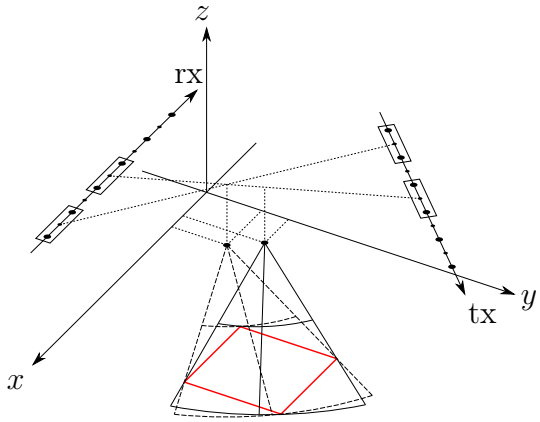

(c) Two subapertures and their elliptical grids and origins

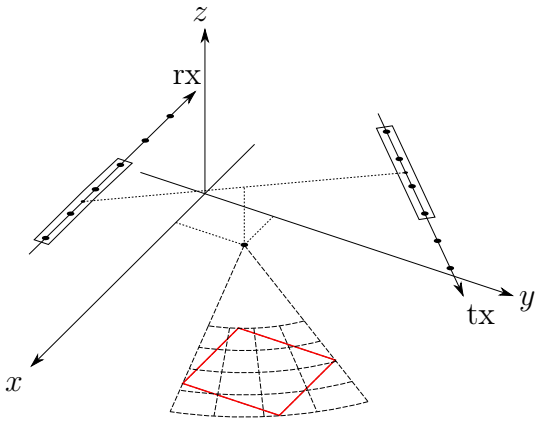

(d) The merged image with the new grid and origin for the larger subaperture

Figure 2.16: First steps in the procedure of FFBP

3
Simulation

The simulation has been implemented in Matlab as described and derived in Chapter 2. This will include physical aspects such as the far-field pattern of the transmit and receive antennas, and free-space loss. Further physical aspects, the effect of antenna coupling, reflections from the metallic tower, and advanced simulations of the forest will not be included as these effects have been evaluated as not contributing much to the understanding of the problem while adding at lot of complexity. The forest is modelled as a cloud of point scatterers. This is sufficient as the goal is not to accurately model forest scattering, which is not a trivial task [4].
This chapter first discusses the antenna pattern implementation, then the monostatic geometry with details of resolution, ambiguities, and windowing. Further on the bistatic geometry and related differences are presented.

3.1 Antennas

For parts of the simulation, in particular troubleshooting and verification, isotropic antennas are used. Which are easy to implement as $A_{tx}A_{rx} = 1$ in eq. (2.9). All antennas are polarized, most commonly linearly, and the BorealScat project is set up to investigate the different combination of horizontal (H-pol) and vertical polarization (V-pol). All combinations are HH, VV, HV and VH. For most cases HV and VH will produce the same results, but not for the P/L-band antenna arrays as they are offset compared to each other.

3.1.1 Antenna pattern

In order to simulate more realistic results the antenna patterns need to be simulated. The antennas are commercial so the simulated patterns will depend on data supplied by the manufacturers.
Due to the fact that the simulated targets are of point-like nature, only the far-field value of the antenna in the exact direction of the target is needed. This is the case for both the receive and transmit antenna, and therefore the antenna pattern term in the theoretical formulation becomes a multiplication of two complex numbers, the A_{tx} and A_{rx}, for each triad of transmit antenna, scatterer, and receive antenna.

3.1.1.1 P/L-band

The P/L-band antennas are log-periodic dipole arrays manufactured by Rohde & Schwarz. The antennas have a single polarisation therefore two are used for each

transmit/receive, as described in Chapter 2. The data supplied by the manufacturer is in form of a FEKO (electromagnetic full-wave simulator) far-field file. The data was evenly spaced on a spherical coordinate system, and by exploiting the periodic nature of this data interpolation to any arbitrary angle can be done.
No antenna truly has a single polarisation, a horizontally polarised antenna will transmit/receive some power on the vertical polarisation. As the point scatterers in the simulation are totally reflective the only HV and VH part will be from this cross-polarisation leakage.

3.1.1.2 C-band

The C-band antennas are manufactured by Cobham, and the data for them is not the complete far-field sampled over an entire sphere as was the case with P/L-band. Instead only a horizontal and a vertical cut of the far-field is supplied. In order to reconstruct an approximation of the field in any relevant direction the Product algorithm as described in [44] is used. This algorithm is simple and relies on the separability of elevation and azimuth, which often is a good approximation for the main lobe.

3.2 Monostatic Geometry

For the development and evaluation of the algorithms a few different monostatic arrays where used. To test the computational complexity of both GBP and FFBP, a linear array of varying number of elements was used. When generating images, both from simulated and measured data, the virtual phase array described in Section 2.2 will be truncated to the closest lower number that is a power of two, 16. The resulting array is shown in Figure 3.1. For the tower's geometry and a monostatic setup no care needs to be taken between the slant-range plane and the image plane as they coincide.

3.2.1 Range Resolution and Ambiguities

The resolution in range is determined by eq. (2.11) and is listed in Table 3.1. The unambiguous range is determined by eq. (2.13), which with the system $\Delta f = 0.5$ MHz results in 300 m. This presents no problem, as scatterers at that distance return such a weak signal that they disappear in the noise of the physical system. In elevation the resolution and unambiguous distance is determined by eq. (2.12) and eq. (2.14) respectively. Due to the dependence on range, three example ranges are used in calculating these metrics in Table 3.2. The truncated array is used.
The C-band will provide the best resolution in range due to larger bandwidth, but only second best in elevation resolution. This is because of the shorter extent of the C-band antenna array, compared to the P/L-band array. A better elevation resolution could have been achieved by separating the elements more, extending the total array length. The compromise is that the unambiguous elevation would shrink. The range and elevation resolution at range 20 m is illustrated in Figure 3.3a

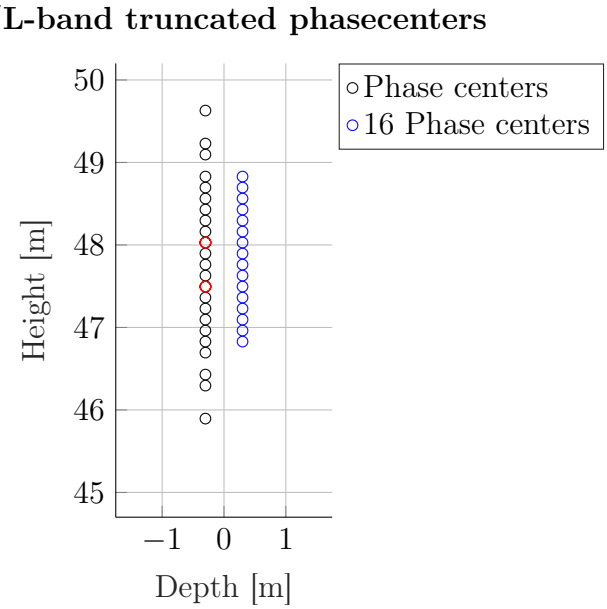

Figure 3.1: The truncation from 25 virtual phase centres down to 16. As before the red rings indicate two virtual phase centres that overlap. Note that the offset in depth is simply done to better illustrate which phase centres are kept, and no actual offset in depth is made in the simulation.

Table 3.1: Range resolution for the defined frequency bands

Frequency band		B [MHz]	Range resolution [m]
P-band	1	30	5.0
	2	8	18.8
	3	8	18.8
	4	56	2.7
L-band	5	135	1.1
C-band	6	320	0.47

Table 3.2: Elevation resolution and unambiguous distance for the frequency bands at a range of 20 m, 50 m and 100 m, with the truncated virtual phase centre array.

		Elevation Resolution [m]			Ambiguity [m]		
Range [m]		20	50	100	20	50	100
P-band	1	3.5	8.6	17.2	52	130	259
	2	2.9	7.3	14.6	44	110	219
	3	2.8	6.9	13.7	41	103	207
	4	2.3	5.9	11.7	35	88	176
L-band	5	1.2	2.9	5.7	17	43	86
C-band	6	1.3	3.5	6.9	21	52	105

Illustrating ambiguities in Figure 3.2a where a straight line of point scatterers at the same height as the array causes ambiguities to appear at a clockwise rotation in the image where no actual scatterers are located. Figure 3.2b shows that simulating scatterers at these ambiguous positions similarly causes ambiguities at the original locations.

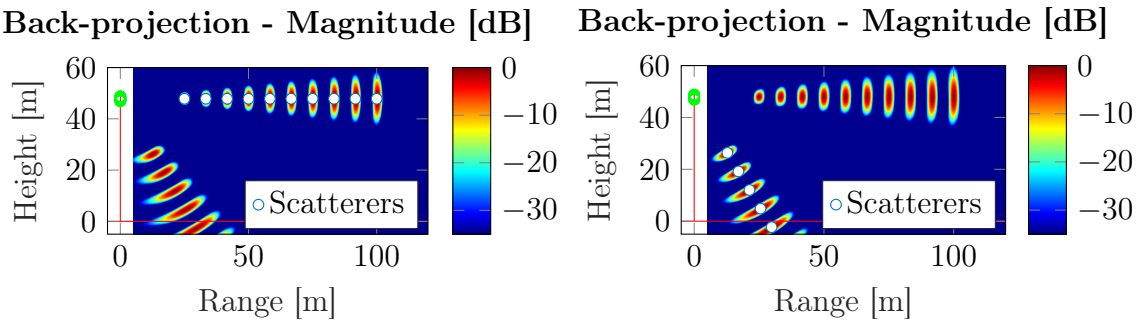

(a) A line of scatterers at the same height as the truncated linear array.

(b) The scatterers extending in a line rotated 60° from boresite.

Figure 3.2: Ambiguities in the geometry of the tower. The red lines in the plots represents the tower and the ground, while the green circles are the antenna positions.

3.2.1.1 Windowing

A strong point scatterer causes large sidelobes in both range and elevation, which is simulated in Figure 3.3a. In order to get more visually identifiable scatterers a reduction in sidelobe level is desirable, therefore windowing will be applied in both range and azimuth. A downside with reducing the sidelobes is that the mainlobe will broaden, a broadening that depends on the amount of sidelobe suppression.
Range windowing is achieved by applying a Hamming window on the frequency data before inverse Fourier transform. This window was chosen because of the reasonable trade-off between sidelobe suppression and mainlobe broadening. In elevation the window is applied as a factor to each of the range profiles before the tomographic reconstruction. For the elevation the window will be a Taylor window. The difference comes from the fact that the number of samples in elevation are much fewer and as to not lose too much resolution the Taylor window with parameters nbar = 3 and sidelobe level −30 dB is used. The effects of windowing is illustrated in the four images in Figure 3.3.

3.2.2 Fast Factorised Back-Projection

To test the FFBP implementation and to show that there is a speedup compared to GBP, an N^2 image with N aperture points will be simulated for several values of N. The result is plotted in Figure 3.4, from which one can see that FFBP is always faster than GBP. The one labelled FFBPqa is the same as FFBP but with a higher azimuth oversampling in order to create a better image. This can be seen to have

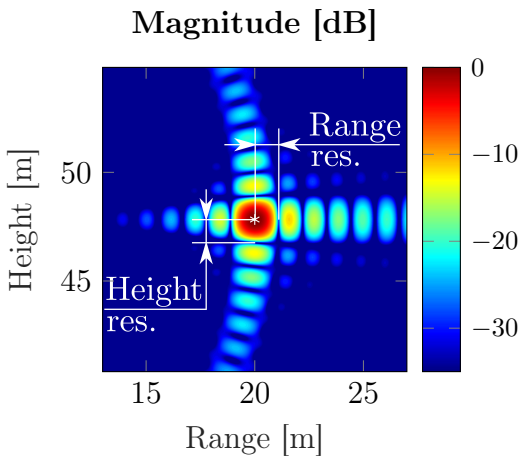

(a) A single scatter located at a range of 20 m as the same height at the middle of the array. No windowing has been applied and large sidelobes are evident.

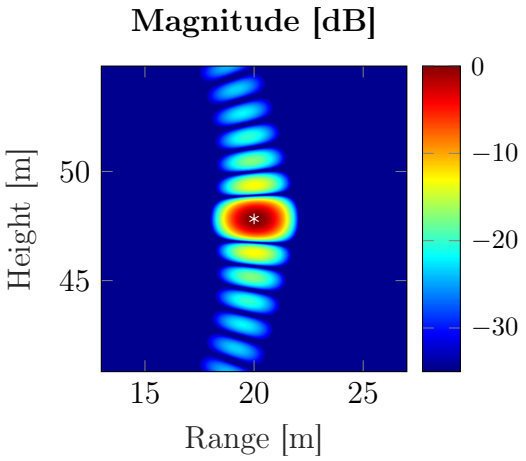

(b) Hamming window applied in range.

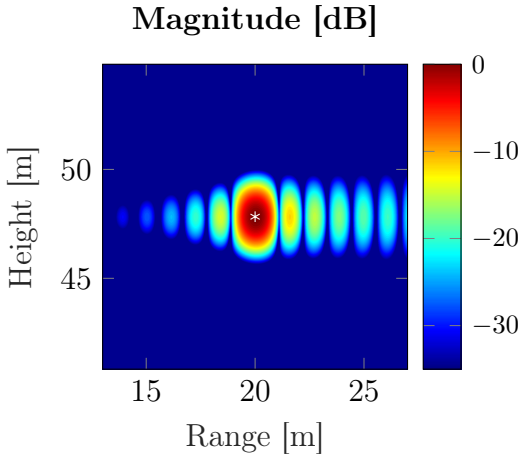

(c) Taylor window applied in elevation

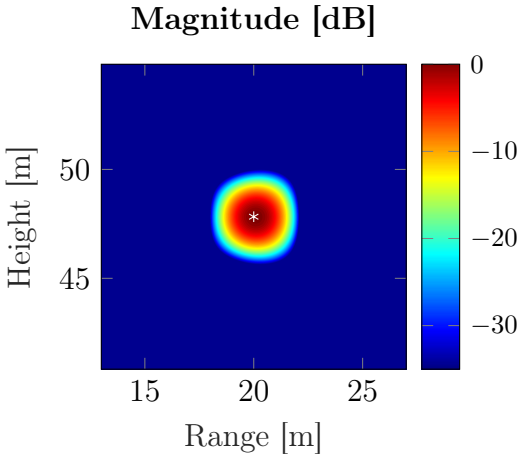

(d) Both windows applied, a broadening of the reconstructed scatterer in both dimensions are evident.

Figure 3.3: Showing the effects of windowing on the sidelobes of a single scatterer simulated at L-band with the truncated virtual phase array, and constructed with GBP

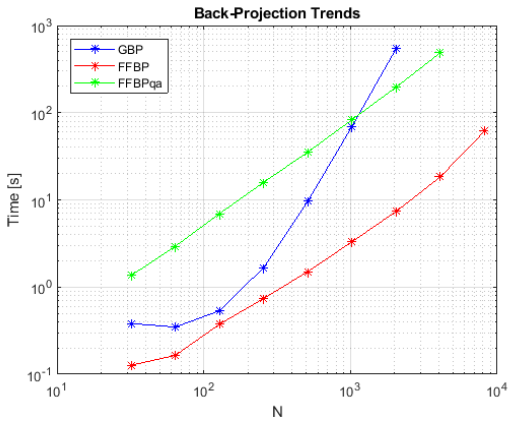

Figure 3.4: The increase in computation time as a function of aperture size, N, when creating a N^2 image. The blue is the ordinary GBP, the red is FFBP with an oversampling of two in azimuth of the first stage and using linear interpolation, and to contrast the green is the same but with a first stage oversampling of 32.

the same effect as creating a larger image without oversampling but otherwise the computational complexity is the same.
The big $\mathcal{O}$ concept only takes into account the general trend of computational time compared to input size, therefore there will be some discrepancies with that and the presented graph. For example, the bookkeeping need to keep track of pixels in different coordinate systems is probably higher for FFBP compared to GBP, this probably contributes to the nonlinearity in the lower N of GBP and FFBP. The contradictory reduction of time with larger N for GBP, is due to the fact of large difference in the sub-second execution times for these. Sometimes as large as a factor 2-3, and only 10 runs where averaged. Other things that can change the complexity is if different interpolators are used. However, the results fit fairly well with the theoretical predictions with GBP having a slope of just below three corresponding to a complexity of $\mathcal{O}(N^3)$, and FFBP just below two which corresponds to $\mathrm{N}^2 \log_2 \mathrm{N}$. The lower slope than three and two can be explained that the bookkeeping and surrounding code take up a larger percentage of time at lower N, thus causing a lower slope. Also the $\log_2 N$ term for FFBP would be hard to notice in these results as it would be drowned out by the other mentioned effects. Finally these results should not be viewed as a validation of the theory, but rather as a verification of the implementation.

3.3 Bistatic Geometry

For more general geometries the monostatic approximation will prove to be inaccurate. For example if the range is short compared to the reconstructed image size.
The general bistatic geometry introduces a double square root term in the azimuth-range signal space. An analytical solution exists for the monostatic case which only has one square root term, the one that causes what is called the hyperbolic range walk [13], but that is not the case with the double square root term. This causes

problems when developing frequency domain algorithms [38].
In the context of back-projection the largest differences between monostatic and bistatic SAR is that instead of projecting range profiles over spheres one needs to do it over ellipsoids [45].
In regards to the tower a change to bistatic geometry also implies three dimensions. An example of the antenna configuration for P/L-band HH polarisation is shown in Figure 3.5. Extending the GBP implementation in this case is trivial as only the

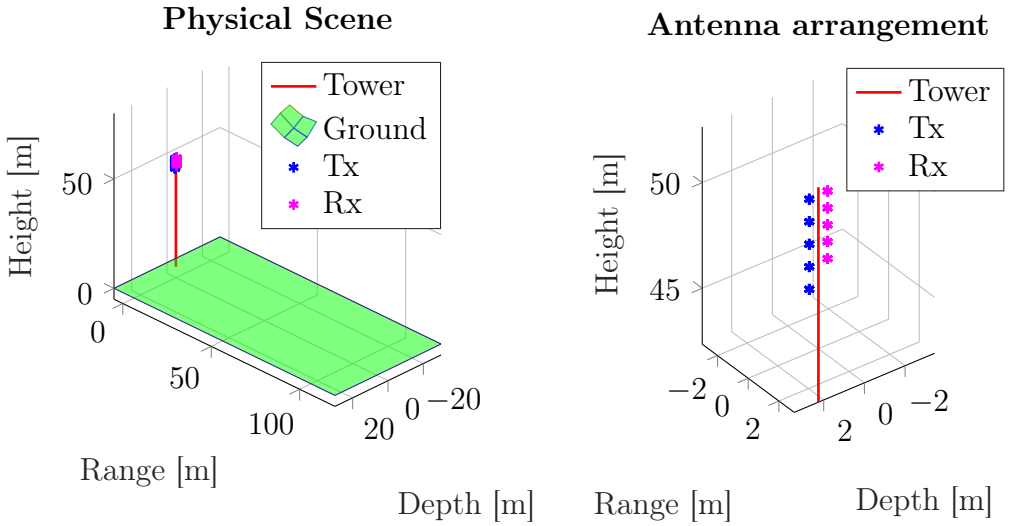

(a) Overview of the geometry in the bistatic case, with the tower in red, transmit and receive antennas in blue and magenta respectively, and the ground in cyan.

(b) Close-up of the antenna geometry.

Figure 3.5: The bistatic setup of the tower geometry for the HH-polarised P/L-antenna arrays.

calculations for the time delay changes, as explained in Section 2.8.1.
The extension of FFBP to BiFFBP, is not as straight forward. And unfortunately due to time constraints a working version of BiFFBP was not able to be implemented.

4

Results

It should be noted that with the simulated results distortions such as shadowing, i.e. not being able to image scatterers behind larger ones, is not taken into account in the simulated images due to the Born approximation.
The results from the monostatic reconstruction of both simulated and measured data is presented first, followed by partial bistatic reconstruction of simulated data. Ending with details about range compensation.

4.1 Monostatic Approximation

The monostatic (virtual phase centres) approximation as first mentioned in Section 3.2 is valid for large ranges and that the transmitter is fairly close to the receiver, i.e. the plane wave approximation [39]. It should be noted that it is only an approximation of range, and not for the actually scattered field.

4.1.1 Simulated Forest

The forest is simulated as a collection of point scatterers within a volume as illustrated in Figure 4.1.

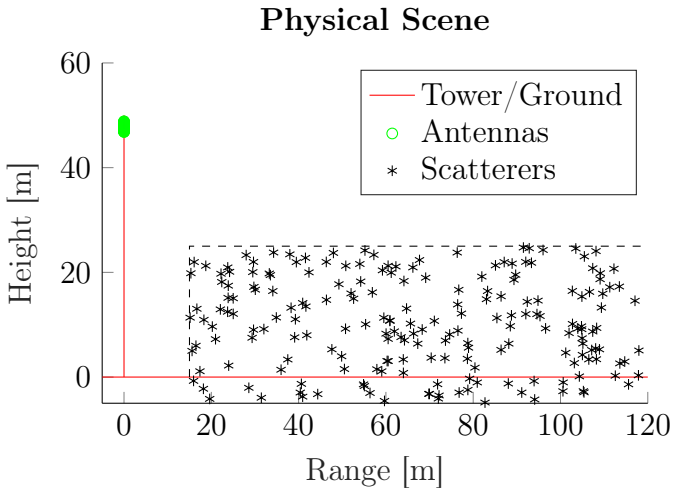

Figure 4.1: The simulated forest scene using 200 randomly distributed point scatterers in the area where the forest is expected to be.

Plots with reconstructed images from the simulated forest for three bands and both

GBP and FFBP is shown in Figure 4.2. For the most part these results can be called equivalent for GBP and FFBP, except for large angles where the FFBP implementation has some issues. This is visible at close range, looking at 5 m range close to the ground where the FFBP implementation produces low values, whereas GBP gives much higher values.
Another issue that has been mentioned is the one of ambiguities, which are apparent in the reconstructions at L- and C-band in Figure 4.2. These are not a problem, as it is evident that the forest does not stop to reflect for the region 30 m to 40 m to then start again. The results are simulated with the truncated array, which highlights the ambiguity problems further.

4.1.2 Antenna Effects

To illustrate the effect of the antenna pattern, the same scene is reconstructed with the pattern as well as with isotropic radiators. Both are plotted in Figure 4.3. There is a clear decrease in the intensity of the backscatter from the point cloud beyond the -3 dB limit in Figure 4.3b, as compared to Figure 4.3a with isotropic radiators. The effects will be similar for C-band, although the C-band antenna array is tilted down towards the forest. Reasons for why the P/L-band antennas are not is explained in [3]

4.1.3 Measured Data

In order for reconstructed images from measured data to be well-focused the exact phase of the received signals in relation to the physical antennas are needed, but this is not the case and during the image reconstruction these errors causes distortions in the image, such as blurring. Therefore an auto-focusing procedure is used to create images with the best focus. It works by making small adjustments to the phase between signals in order to increase the contrast. This is a nonlinear optimisation problem and is currently solved by a particle swarm optimisation algorithm, followed by a hill climbing routine involving many iterations. This results in a fairly large amount of images being generated, and at the current state the entire process takes longer than the five minute interval of data being captured [3]. This is not a part of this thesis, so for demonstrating the use of the algorithms the measured data will already be preprocessed.
The result of using GBP and the entire virtual phase array for P-band, one L-band, and the C-band is plotted in Figure 4.4. The images are focused, but one problem with the focusing processing is that it causes an arbitrary rotation in the images. Perhaps most clearly illustrated in the L-band image, Figure 4.4b, where a reflector which in reality is located on the ground hovers at a height of about 20 m. Forest features such as canopy can be identified, but is also rotated.
To use the FFBP to compare with GBP the reduced number of range profiles, 16, will be used. These corresponds to the same as in the reduced virtual phase centre in Section 3.2. These results are plotted in Figure 4.5. Again GBP and FFBP produce the same result, except for large angles.
To compare the speedup for reconstruction of the different images, the computational

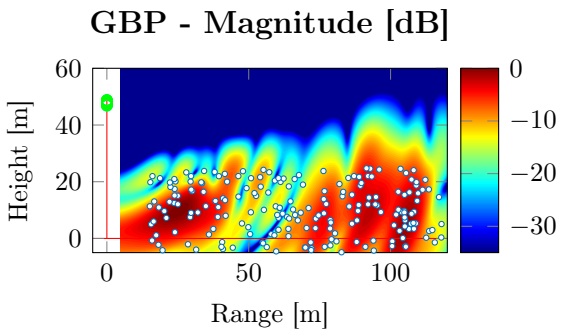

(a) P-band reconstruction using GBP

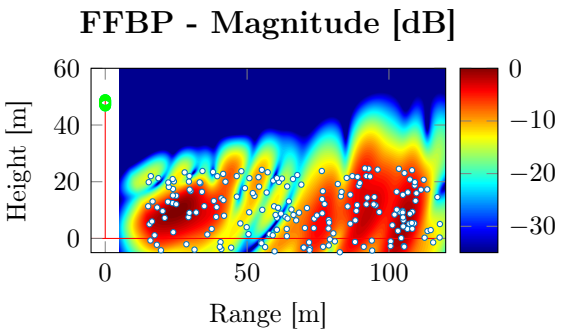

(b) P-band reconstruction using FFBP

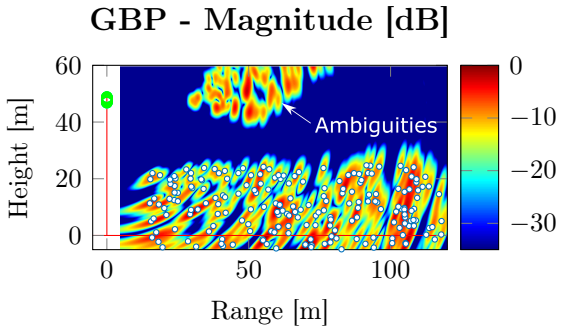

(c) L-band reconstruction using GBP. Ambiguities are visible.

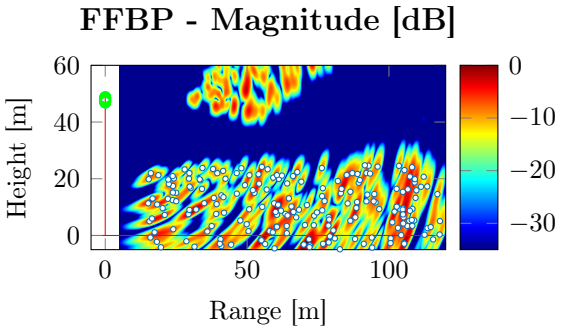

(d) L-band reconstruction using FFBP

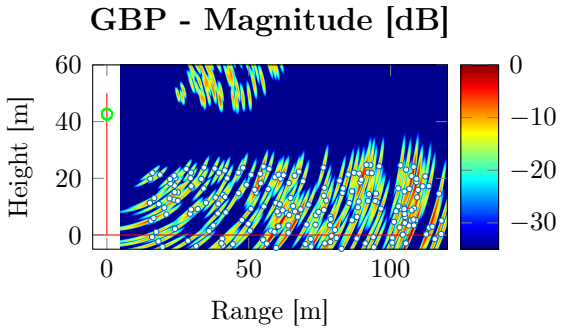

(e) C-band reconstruction using GBP

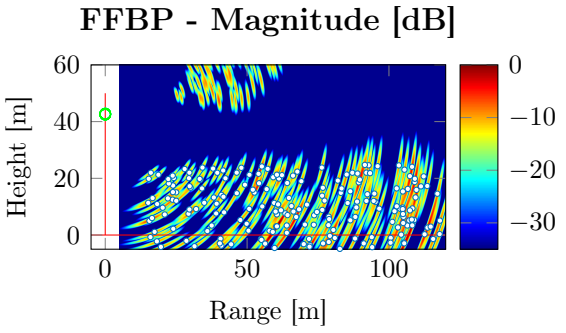

(f) C-band reconstruction using FFBP

Figure 4.2: Comparison of reconstructed images with GBP and FFBP with reduced aperture size. All reconstructions use four times oversampling in range and linear interpolation, while the FFBP images also use 16 times oversampling in elevation.

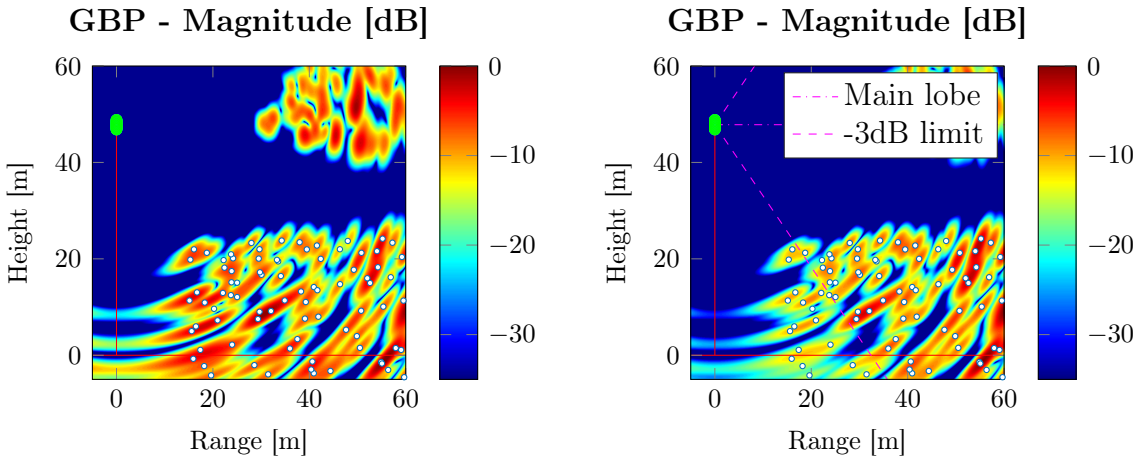

(a) L-band reconstruction with isotropic antennas and truncated array.

(b) L-band reconstruction with the modelled P/L-band antennas and truncated array, with HH polarisation.

Figure 4.3: Comparing the impact of the P/L-band antenna pattern against isotropic pattern.

time is listed in Table 4.1. These times have been averaged over four reconstructions of each image. As mentioned in Section 2.4 due to the fact that the number of

Table 4.1: Comparison of computation time for GBP and FFBP images when using the measured data for the different bands. For both algorihtms the range profiles where oversampled with four times the closest power of two, and for FFBP there was a 16 times oversampling in elevation.

Frequency band		Nr of range samples	Image size [Mpx]	GBP time [s]	FFBP time [s]	Speedup t_{GBP}/t_{FFBP}
P-band	1	1k	2.31	4.11	2.76	1.49
L-band	5	8k	2.31	4.50	2.68	1.68
C-band	6	16k	2.31	4.07	2.82	1.45

aperture points are far fewer than the number of pixels the speed up will not be as high as for the idealistic case of N aperture points for an N^2 image. However, it is evident that a speedup with FFBP is realisable.

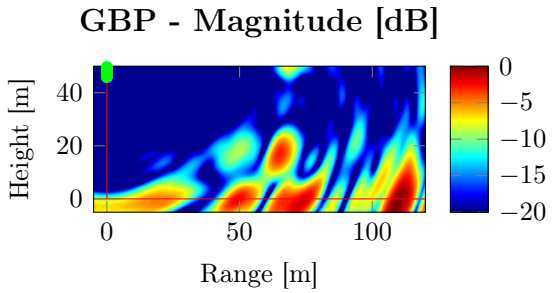

(a) P-band reconstructed with GBP

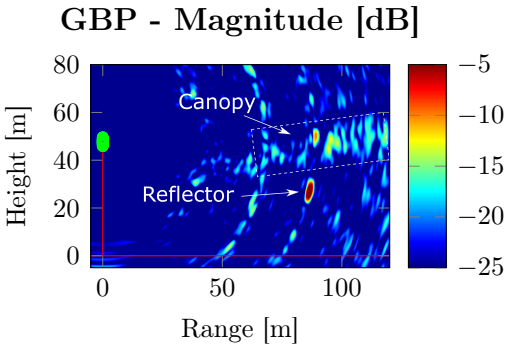

(b) L-band reconstructed with GBP

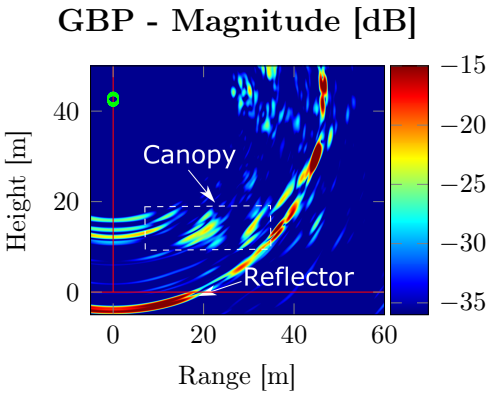

(c) C-band. The shortest range plotted because little of the radiation penetrates the forests foliage.

Figure 4.4: Reconstruction of images from already focused data using GBP, with four times oversampling in range and linear interpolation. An arbitrary rotation can be seen in the images, which comes from the focusing procedure. The L-band and C-band shows less in range, due to higher frequencies penetrating less into the forest canopy.

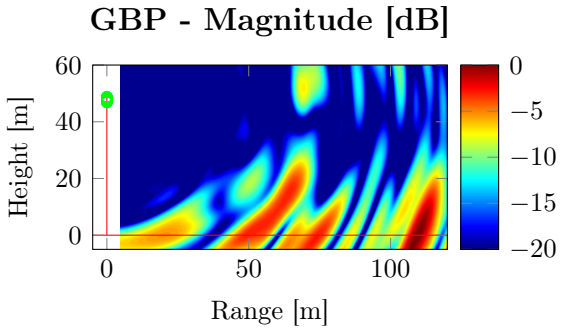

(a) P-band using GBP

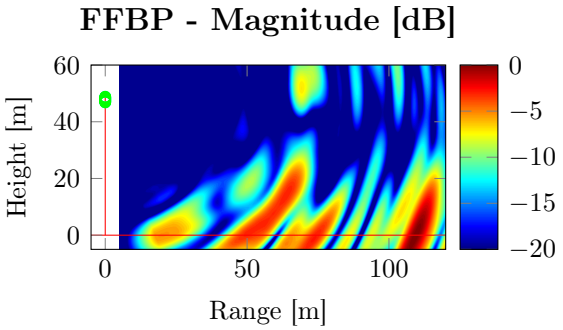

(b) P-band using FFBP

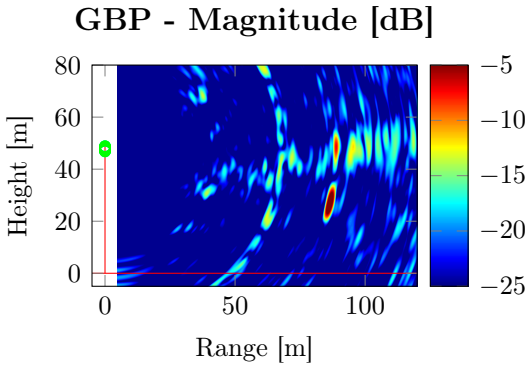

(c) L-band using GBP

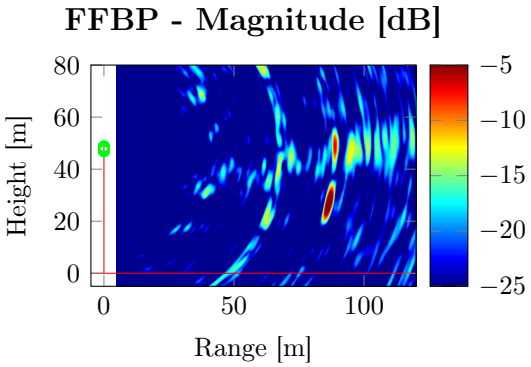

(d) L-band using FFBP

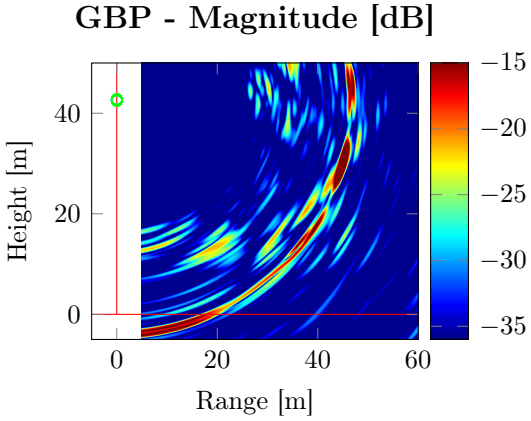

(e) C-band using GBP

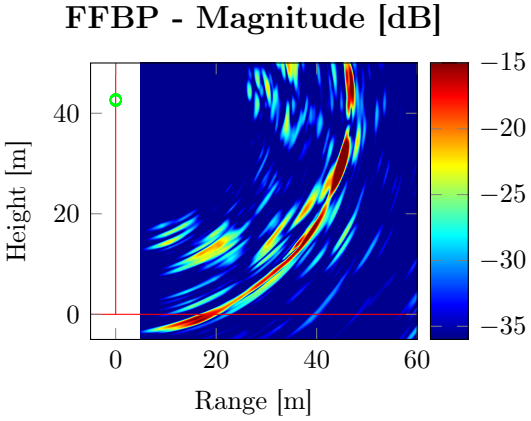

(f) C-band using FFBP

Figure 4.5: Comparison of reconstructed images with GBP and FFBP with reduced aperture size. All reconstructions use four times oversampling in range and linear interpolation, while the FFBP images also use 16 times oversampling in azimuth.

4.2 Bistatic Geometry

As mentioned in Section 3.3 time constraints put a stop to the implementation of BiFFBP. However, the simpler bistatic GBP will be demonstrated with an arbitrary geometry in two dimensions, as well as the steps that have been taken in the implementation of BiFFBP.

As detailed in Section 2.8.1 only a slight modification is needed to accommodate bistatic geometries in the formulation of GBP. In Figure 4.6 a scene with point scatterers located in a 3D volume is illustrated. Range profiles are generated with the truncated bistatic arrays and images are reconstructed with GBP both for the true bistatic geometry, in Figure 4.6b, and with the monostatic virtual phase array in Figure 4.6c. Taking the difference in dB (i.e. same as quotient in linear) between the these reconstructions gives a metric of how similar they are, and is plotted in Figure 4.6d. The desired result is to have values as close to zero as possible, and for the region where the scatterers are located this is true, therefore the conclusion is that the monostatic virtual phase centre approach is valid. The large difference in the sidelobe levels above the forest at a range of 100 m is not easily explained. One cause could be issues with the implementation. Note also that only the magnitude is compared here, any differences in phase is not evaluated.

The partial progress that has been made for BiFFBP is in terms of a testing geometry, as visualised in Figure 4.7a. To easier develop and troubleshoot the algorithm only one step in the factorisation is done. This is accomplished by construction two images using GBP and half the array for each image, and then combine these with BiFFBP. Thereby simulating the last step in the factorisation. In Figure 4.7b and Figure 4.7c these two halves are plotted. These must be in the elliptical coordinate system, as described in Section 2.8.2, for the BiFFBP algorithm to be able to merge them.

The result of the final step in the factorisation is plotted in Figure 4.8b. As a reference, the same image reconstructed with GBP is plotted in Figure 4.8a. Some differences are apparent, primarily that the upper left corner is weaker and that the lower right corner is stronger for the BiFFBP image. This might not appear to be significant, however, with multiple steps in the factorisation these errors accumulate and distorts the image beyond usability.

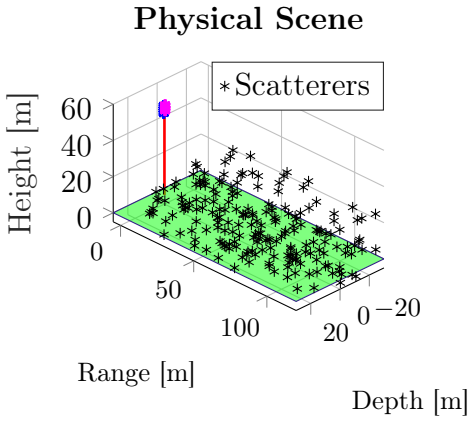

(a) The physical scene with the cloud of point scatterers representing the forest.

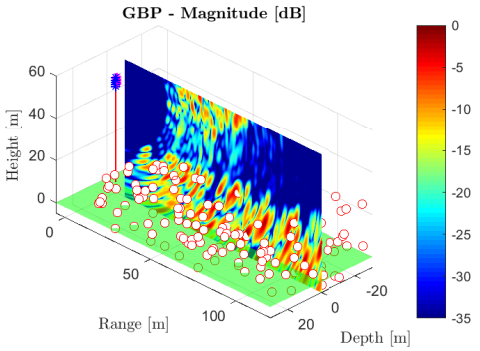

(b) Reconstruction of the scene with the truncated bistatic array using GBP.

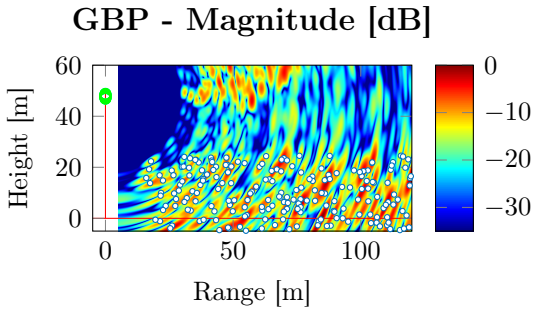

(c) Reconstruction of the same image using the same range profiles but the virtual phase centres as antenna locations instead.

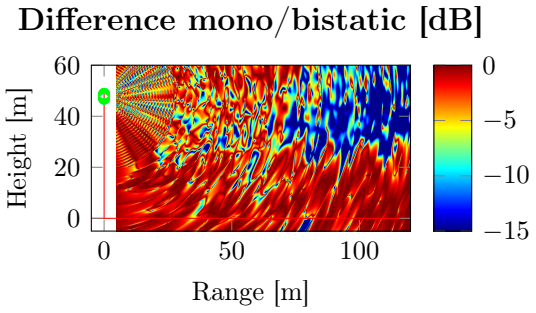

(d) The difference in dB between the virtual phase center (monostatic) and the bistatic reconstruction. Values close to zero indicates little difference between them.

Figure 4.6: Reconstruction of images with GBP in 3D, compared to the monostatic approximation 2D GBP.

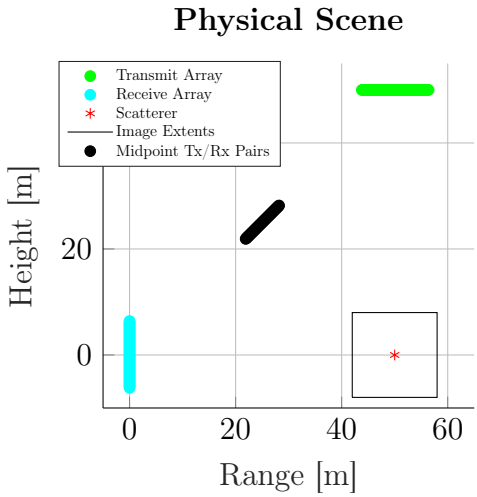

(a) Testing scene used in the development of BiFFBP.

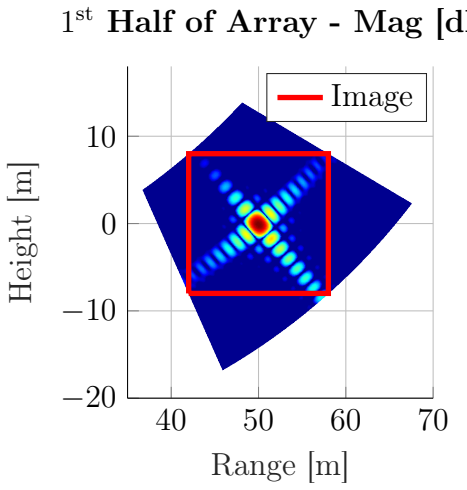

(b) GBP image reconstructed from the first half of the array. The elliptical coordinate system is used.

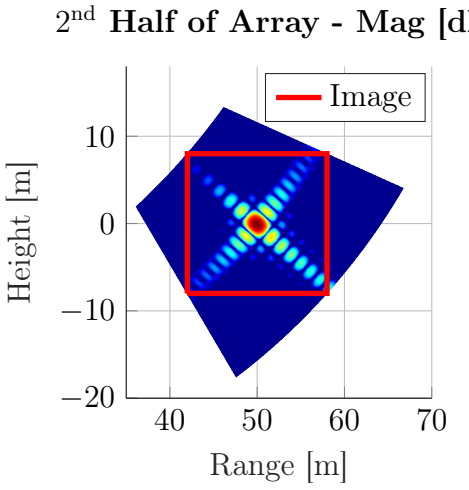

(c) GBP image reconstructed from the second half of the array. The elliptical coordinate system is used.

Figure 4.7: Setup for testing and developing the BiFFBP algorithm.

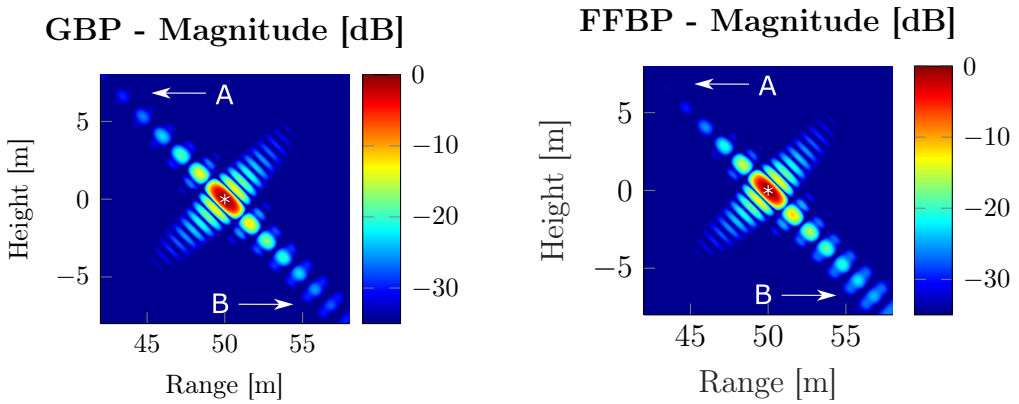

(a) Full reconstruction using GBP.

(b) Reconstruction using BiFFBP using the two halves in Figure 4.7.

Figure 4.8: Comparing the reconstruction using GBP and one step of BiFFBP. The labels A and B are to point out the largest differences.

4.3 Range compensation

Due to the free-space propagation loss the voltage amplitude of the received signal will be reduced by a factor $1/(4\pi r)^2$, where r is the distance to the scatterer. As to remove this effect the range profiles are multiplied with $(4\pi r)^2$ with the relevant r for each range bin. This fixes the free-space loss, but it introduces an image distortion in terms of a spatial shift in the reconstructed image, such that the peak of the magnitude no longer coincide with where the scatterer is located. This is illustrated in Figure 4.9, with the comparison of the same image with and without range compensation.
The reason for this phenomena can be made more apparent by looking at an example scatterer at distance r which generates the back scatter plotted in Figure 4.10a. The peak, range r, is multiplied with the factor $(4\pi r)^2$, while at a distance Δr away from the peak the factor will be $(4\pi(r \pm \Delta r))^2$. In order to have a small shift of the peak the ratio between the factor at the peak and at $\pm\Delta r$ should be close to 1. The ratio is

$$\begin{aligned} A &= \frac{(4\pi r)^2}{(4\pi(r \pm \Delta r))^2} \\ &= \left(\frac{r}{r \pm \Delta r}\right)^2 \\ &= \left(1 \mp \frac{\Delta r}{r \pm \Delta r}\right)^2 \end{aligned}$$

From which it can be seen, that in order to have a small shift the range r should be large or Δr small. For radar the case is often the first one, that the distances are large, while the second case means a larger bandwidth for the same level at Δr.
Another problem is that the amplification of sidelobes, which for scatterers close to the array can become significant further away, which can be viewed in the compensated range profile in Figure 4.10b. This shows that it is not impossible to have

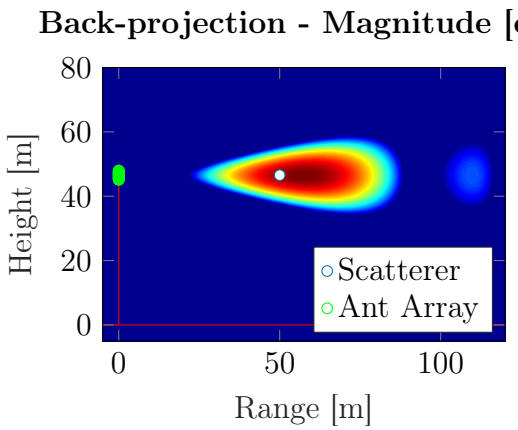

(a) A reconstructed image showing offset between the scatterer and the peak of the reconstructed image due to range compensation.

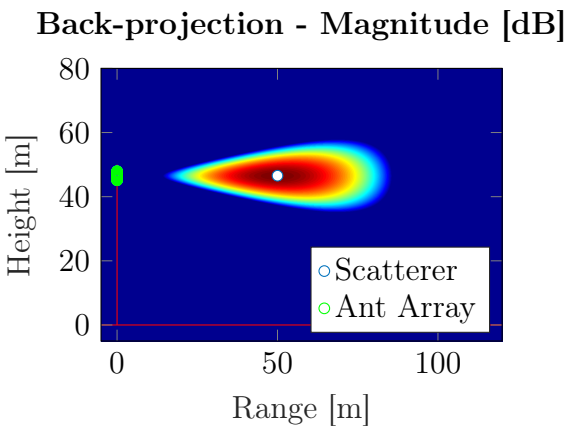

(b) Without range compensation the peak of the reconstructed image is at the same location as the scatterer.

Figure 4.9: Showing the difference between reconstruction with and without range compensation. The effect is most pronounced at short range and with small bandwidth, here the simulated bandwidth is 8 MHz at 546 MHz. The sidelobes are suppressed with windowing.

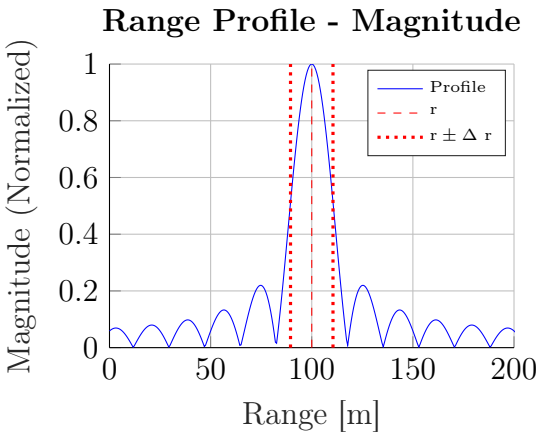

(a) The range profile from the scene of a single scatterer with the use of a band limited signal. The r indicates the peak of the sinc while Δr is a small arbitrary offset, here the -3 dB point.

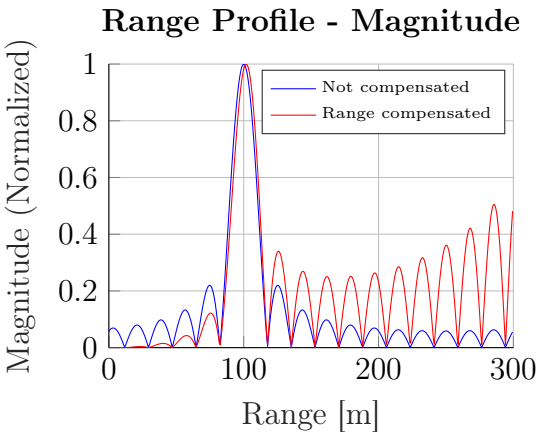

(b) Comparison between a compensated versus uncompensated range profile, showing the range offset, and also the the amplification of sidelobes.

Figure 4.10: Showing the effect of range compensation on range profiles with a single scatter located 100 m away from the antennas. In **(b)** the amplification of sideslobes are also evident.

sidelobes be amplified above the level of the actual mainlobe, however, it causes distinct ringing artefacts in a reconstructed image which are easily identifiable.

5
Conclusion

The goal of implementing a faster reconstruction algorithm than GBP has been accomplished in the monostatic approximation via FFBP, and the speedup is of the expected order. About 50% - 70% for the tested scenarios, compared to the theoretical maximum speedup of four times. Reduced accuracy at large angles is seen in the implementation, however, as long as this is taken into consideration the results of the algorithms are considered to be equivalent. The bistatic version of FFBP has been partially implemented, unfortunately not entirely completed. There are no apparent reasons why BiFFBP would not be able to reconstruct tomographic images and therefore speedup also the bistatic geometries.
For the FFBP algorithms to be of practical use information should not be discarded as has been the case for a majority of the reconstructed images in this thesis. Instead a more advanced version ought to be implemented that uses one or more of the ideas presented in Section 2.8.2.
The problems introduced by range-compensation in terms of shifting of the scatter location in the reconstructed image, does not have to be a problem. However, for the geometries such as the tower's and especially in combination with low bandwidth one needs to be aware of these issues. Further, one has to be careful when interpreting the reconstructed images if there are possibilities for ambiguities, as are the case for several of the images presented in this thesis.

5.1 Other considerations

Another approach to increase the speed of reconstruction could be to simply parallelise the existing algorithm. This approach is not an efficiency improvement as the same number of instructions are being executed, however, due to the fact that most modern computer systems have multiple computational units in some way it is often a fairly easy route to go to achieve some speedup. This assumes that the algorithm in question can be executed in parallel, which is not always the case.
The parallelisation of GBP is straightforward, because each range profile is treated separately and distributed over the image. For example in Matlab it might be as easy as switching `for` with `parfor`. One could also utilise the general availability and high power of modern computer graphic cards, which has been done [46, 47]. The best thing would be to combine both a faster algorithm with parallelisation to get the advantage of both.
A more radical option would be to look into the developments of frequency-domain algorithms that have been specifically tailored towards bistatic geometries, one ex-

ample being Non-Linear Chirp Scaling (NLCS) [38].

5.2 Future Work

For the future, the first step is to complete the unfinished parts in the bistatic implementation of BiFFBP, and apply it to the tower geometry and data.
It would also be interesting to implement the solutions in a compiled language, such as C, to see whether further speed gains could be achieved. A look at a GPU implementation might also be worthwhile.
Closer investigation of optimum oversampling in range and elevation in terms of maximum speedup, also in relation to using other kinds of interpolators, such as nearest neighbour. Also generally optimising the Matlab code for maximum speedup.

Bibliography

[1] IPCC, "Climate change 2014: Synthesis report", IPCC, Geneva, Switzerland, 2014. [Online]. Available: https://www.ipcc.ch/report/ar5/syr/ (visited on 01/23/2018).

[2] European Space Agency, "Report for Mission Selection: BIOMASS, ESA SP-1324/1", European Space Agency, Noordwijk, The Netherlands, 2012. [Online]. Available: https://earth.esa.int/web/guest/document-library/browse-document-library/-/article/biomass-report-for-mission-selection-an-earth-explorer-to-observe-forest-biomass (visited on 01/24/2018).

[3] A. Monteith, "Radar measurements of temporal variation in a boreal forest", Lic. thesis, Department of Space, Earth and Environment, Chalmers University of Technology, Gothenburg, Sweden, 2018.

[4] B. Hallberg, "Synthetic-aperture radar imaging of forests in the VHF and UHF bands, Electromagnetic models and data analysis", Ph.D. thesis, Rymd o geo, Chalmers University of Technology, Gothenburg, Sweden, 2007.

[5] E. S. Agency. (2017). ESA future missions, Biomass, [Online]. Available: https://earth.esa.int/web/guest/missions/esa-future-missions/biomass (visited on 05/15/2018).

[6] C. Albinet *et al.*, "TropiSCAT, A ground based polarimetric scatterometer experiment in tropical forests", *IEEE Journal of Selected Topics in Applied Earth Observations and Remote Sensing*, vol. 5, no. 3, pp. 1060–1066, Jun. 2012. DOI: 10.1109/jstars.2012.2201917. [Online]. Available: http://ieeexplore.ieee.org/document/6216452/ (visited on 02/01/2018).

[7] C. Albinet *et al.*, "First results of AfriScat, a tower-based radar experiment in africa forest", in *2015 IEEE International Geoscience and Remote Sensing Symposium (IGARSS)*, Milan, Italy, Jul. 26–31, 2015, pp. 5356–5358. [Online]. Available: https://ieeexplore.ieee.org/document/7327045/ (visited on 05/16/2018).

[8] H. Hertz, "Ueber electrodynamische wellen im luftraume und deren reflexion", *Der Physik und Chemie*, vol. 270, no. 8a, pp. 609–623, Nov. 1888. DOI: 10.1002/andp.18882700802. [Online]. Available: https://onlinelibrary.wiley.com/doi/abs/10.1002/andp.18882700802 (visited on 05/29/2018).

[9] G. Galati, *100 Years of Radar*. city, PA, USA: Springer International Publishing, 2016. [Online]. Available: https://link.springer.com/book/10.1007%2F978-3-319-00584-3 (visited on 05/29/2018).

[10] S. S. Swords, *Technical History of the Beginnings of Radar*. Herts, United Kingdom: The Institution of Engineering and Technology, 1986.

[11] Emerson. (2018). About non-contacting radar, [Online]. Available: http://www.emerson.com/en-us/automation/measurement-instrumentation/level/continuous-level-measurement/about-non-contacting-radar (visited on 05/29/2018).

[12] C. A. Wiley, "Synthetic aperture radars, A paradigm for technology evolution", *IEEE Transactions on Aerospace and Electronic Systems*, vol. 21, no. 3, pp. 440–443, May 1985. DOI: 10.1109/TAES.1985.310578. [Online]. Available: https://ieeexplore.ieee.org/document/4104077/ (visited on 05/19/2018).

[13] C. F. Barnes, *Synthetic Aperture Radar, Wave Theory Foundations: Analysis and Algorithms*. Powder Springs, GA, USA: C. F. Barnes, 2014.

[14] M. A. Richards, J. A. Scheer, and W. A. Holm, *Principles of Modern Radar, Basic Principles*. Raleigh, NC, USA: Scitech Publishing Inc., 2010, vol. 1.

[15] A. Reigber and A. Moreira, "First demonstration of airborne SAR tomography using mulitbaseline L-band data", *IEEE Transactions on Geoscience and Remote Sensing*, vol. 38, no. 5, pp. 2142–2152, Sep. 2000. DOI: 10.1109/36.868873. [Online]. Available: https://ieeexplore.ieee.org/document/868873/ (visited on 05/17/2018).

[16] L. M. H. Ulander, H. Hellsten, and G. Stenström, "Synthetic-aperture radar processing using fast factorized back-projection", *IEEE Transactions on Aerospace and Electronic Systems*, vol. 39, no. 3, pp. 760–776, Oct. 2003. DOI: 10.1109/TAES.2003.1238734. [Online]. Available: http://ieeexplore.ieee.org/document/1238734/ (visited on 01/23/2018).

[17] W. G. Carrara, R. S. Goodman, and R. M. Majewski, *Spotlight Synthetic Aperture Radar, Signal Processing Algorithms*. Boston, MA, USA: Artech House, 1995.

[18] M. Soumekh, *Synthetic Aperture Radar Signal Processing, with MATLAB Algorithms*. Hoboken, NJ, USA: John Wiley & Sons Inc., 1999.

[19] H. Hellsten, L. M. H. Ulander, A. Gustavsson, and B. Larsson, "Development of VHF CARABAS II SAR", in *Proceedings of SPIE 2747, Radar Sensor Technology*, Orlando, FL, USA, Apr. 8–9, 1996, pp. 48–60.

[20] A. F. Yegulalp, "Fast backprojection algorithm for synthetic aperture radar", in *Proceedings of the 1999 IEEE Radar Conference*, Waltham, MA, USA, Apr. 22, 1999, pp. 60–65. [Online]. Available: https://ieeexplore.ieee.org/document/767270/ (visited on 04/15/2018).

[21] J. McCorkle and M. Rofheart, "An order N2log(N) backprojector algorithm for focusing wide-angle wide-bandwidth arbitrary-motion synthetic aperture radar", in *SPIE Aerospace/Defense Sensing and Controls*, Orlando, FL, USA, Apr. 8–12, 1996, pp. 25–36.

[22] N. J. Willis, *Bistatic Radar*, 2nd ed. Raleigh, NC, USA: Scitech Publishing Inc., 2005.

[23] J. C. Curlander and R. N. McDonough, *Synthetic Aperture Radar, Systems and Signal Processing*. New York, NY, USA: John Wiley & Sons Inc., 1991.

[24] L. Cohen, *Time-Frequency Analysis*. Upper Saddle River, NJ, USA: Pretice-Hall PTR, 1994.

[25] M. Born and E. Wolf, *Principles of Optics, Electromagnetic theory of propagation, interference and diffraction of light*, 7th ed. Cambridge, United Kingdom: Cambridge University Press, 1999.

[26] M. Cheney and B. Borden, *Fundamentals of Radar Imaging*. Philadelphia, PA, USA: Society for Industrial and Applied Mathematics, 2009.

[27] M. I. Duersch, "Backprojection for synthetic aperture radar", Ph.D. thesis, Department of Electrical and Computer Engineering, Brigham Young University, Provo, UT, USA, 2013. [Online]. Available: https://scholarsarchive.byu.edu/etd/4060/ (visited on 05/19/2015).

[28] A. Ribalta, "Time-domain reconstruction algorithms for FMCW-SAR", *IEEE Geoscience and Remote Sensing Letters*, vol. 8, no. 3, pp. 396–400, May 2011. DOI: 10.1109/LGRS.2010.2078486. [Online]. Available: https://ieeexplore.ieee.org/document/5640647/ (visited on 05/21/2018).

[29] J. B. Anderson, *Digital Transmission Engineering*, 2nd ed. Piscataway, NJ, USA: IEEE Press, 2005.

[30] L.-E. Andersson, "On the determination of a function from spherical averages", *SIAM Journal on Mathematical Analysis*, vol. 19, no. 1, pp. 214–232, Jan. 1988. DOI: 10.1137/0519016. [Online]. Available: https://search.proquest.com/docview/924813714 (visited on 05/16/2018).

[31] J. A. Fawcett, "Inversion of n-dimensional spherical averages", *SIAM Journal on Applied Mathematics*, vol. 45, no. 2, pp. 336–341, Apr. 1985. [Online]. Available: http://www.jstor.org/stable/2101820 (visited on 05/16/2018).

[32] A. Olofsson, "Signalbehandling i flygburen ultrabredbanding lågfrekvens-SAR i realtid", M.Sc. thesis, Institution för Radio och Rymdvetenskap, Chalmers University of Technology, Gothenburg, Sweden, 2003.

[33] D. M. Pozar, *Microwave Engineering*. Hoboken, NJ, USA: John Wiley & Sons Inc., 2012.

[34] B. R. Mahafza, *Radar Systems Analysis and Design using MATLAB*, 2nd ed. Boca Raton, FL, USA: Chapman and Hill/CRC, 2005.

[35] M. A. Richards, *Funadamentals of Radar Signal Processing*. New York, NY, USA: McGraw-Hill, 2005.

[36] D. R. Wehner, *High Resolution Radar*, 2nd ed. Norwood, MA, USA: Artech House Inc., 1995.

[37] D. Ho Tong Minh, S. Tebaldini, F. Rocca, T. Koleck, P. Borderies, and C. Albinet, "Ground-based array for tomographic imaging of the tropical forest in p-band", *IEEE Transactions on Geoscience and Remote Sensing*, vol. 51, no. 8, pp. 4460–4472, Aug. 2013. DOI: 10.1109/tgrs.2013.2246795. [Online]. Available: http://ieeexplore.ieee.org/document/6488812/ (visited on 02/01/2018).

[38] Y. L. Neo, "Digital processing algorithms for bistatic synthetic aperture radar data", Ph.D. thesis, Department of Electrical and Computer Engineering, University of British Columbia, Vancouver, Canada, 2007. [Online]. Available: https://search.proquest.com/docview/304707519 (visited on 04/09/2015).

[39] C. V. Jakowatz, D. E. Wahl, and D. A. Yocky, "A beamforming algorithm for bistatic SAR image formation", in *Proceedings of SPIE 7699, Algorithms*

for Synthetic Aperture Radar Imagery XVII, Orlando, FL, USA, Apr. 5–9, 2010, pp. 769902-1–769902-6. DOI: 10.1117/12.851871. [Online]. Available: https://www.spiedigitallibrary.org/conference-proceedings-of-spie/7699/1/A-beamforming-algorithm-for-bistatic-SAR-image-formation/10.1117/12.851871.full (visited on 05/08/2018).

[40] V. T. Vu, T. K. Sjögren, and M. I. Petterson, "SAR imaging in ground plane using fast backprojection for mono- and bistatic cases", in *2012 IEEE Radar Conference*, Atlanta, GA, USA, May 7–11, 2012, pp. 0184–0189. [Online]. Available: https://ieeexplore.ieee.org/document/6212134/ (visited on 05/16/2018).

[41] J. Moll, P. Schöps, and V. Krozer, "Towards three-dimensional millimeter-wave radar with the bistatic fast-factorized back-projection algorithm — potential and limitations", *IEEE Transactions on Terahertz Science and Technology*, vol. 2, no. 4, pp. 432–440, Jun. 2012. DOI: 10.1109/TTHZ.2012.2199113. [Online]. Available: https://ieeexplore.ieee.org/document/6222006/ (visited on 05/08/2018).

[42] Y. Ding and D. C. Munson, "A fast back-projection algorithm for bistatic SAR imaging", in *Proceedings. International Conference on Image Processing*, Rochester, NY, USA, Sep. 22–25, 2002, pp. II-449–II-452. [Online]. Available: https://ieeexplore.ieee.org/document/1039984/ (visited on 05/08/2018).

[43] L. M. H. Ulander, P.-O. Frölind, A. Gustavsson, D. Murdin, and G. Stenström, "Fast factorized back-projection for bistatic SAR processing", in *Proceedings of European Conference on Synthetic Aperture Radar*, Aachen, Germany, Jun. 7–10, 2010, pp. 1002–1005.

[44] T. Petrita and A. Ignea, "A new method for interpolation of 3D antenna pattern from 2D plane patterns", in *2012 10th International Symposium on Electronics and Telecommunications*, Timisoara, Romania, Nov. 15–16, 2012, pp. 393–396. [Online]. Available: https://ieeexplore.ieee.org/document/6408150/ (visited on 03/12/2018).

[45] C. V. Jakowatz, D. E. Wahl, and D. A. Yocky, "A beamforming algorithm for bistatic SAR image formation", *IEEE Transactions on Geoscience and Remote Sensing*, vol. 54, no. 5, pp. 2706–2712, May 2016. DOI: 10.1109/TGRS.2015.2504787. [Online]. Available: https://ieeexplore.ieee.org/document/7361995/ (visited on 05/23/2018).

[46] C. L. Stringham, "Developments in LFM-CW SAR for UAV operation", Ph.D. thesis, Department of Electrical and Computer Engineering, Brigham Young University, Provo, UT, USA, 2014. [Online]. Available: https://scholarsarchive.byu.edu/etd/5587/ (visited on 03/09/2018).

[47] M. Blom and P. Follo, "VHF SAR image formation implemented on a GPU", in *Proceedings 2005 IEEE International Geoscience and Remote Sensing Symposium*, Seoul, South Korea, Jul. 29, 2005, pp. 3352–3356.